UNIVERSITÄT AUGSBURG
Universitätsbibliothek

OPEN ACCESS
OPUS AUGSBURG

ICRF coupling in ASDEX upgrade magnetically perturbed 3D plasmas

G. Suárez López, R. Ochoukov, W. Tierens, M. Willensdorfer, H. Zohm, D. Aguiam, Gregor Birkenmeier, V. Bobkov, M. Cavedon, M. Dunne, H. Faugel, R. Fischer, H. Fünfgelder, L. Guimarãis, R. McDermott, J.-M. Noterdaeme, E. Seliunin, W. Suttrop

Angaben zur Veröffentlichung / Publication details:

Suárez López, G., R. Ochoukov, W. Tierens, M. Willensdorfer, H. Zohm, D. Aguiam, Gregor Birkenmeier, et al. 2019. "ICRF coupling in ASDEX upgrade magnetically perturbed 3D plasmas." *Plasma Physics and Controlled Fusion* 61 (12): 125019. https://doi.org/10.1088/1361-6587/ab47a9.

Nutzungsbedingungen / Terms of use: **CC BY 3.0**

Dieses Dokument wird unter folgenden Bedingungen zur Verfügung gestellt: / This document is made available under these conditions:
CC-BY 3.0: Creative Commons - Namensnennung
Weitere Informationen finden Sie unter: / For more information see:
https://creativecommons.org/licenses/by/3.0/de/deed.de

Plasma Physics and
Controlled Fusion

PURPOSE-LED
PUBLISHING™

PAPER • **OPEN ACCESS**

ICRF coupling in ASDEX upgrade magnetically perturbed 3D plasmas

To cite this article: G Suárez López *et al* 2019 *Plasma Phys. Control. Fusion* **61** 125019

View the article online for updates and enhancements.

You may also like

- Validation of high-fidelity ion cyclotron range of frequencies antenna coupling simulations in full 3D geometry against experiments in the ASDEX Upgrade tokamak
G Suárez López, M Cianciosa, T Lunt et al.
- Simulation of the ion cyclotron range of frequencies slow wave and the lower hybrid resonance in 3D in RAPLICASOL
M Usoltceva, R Ochoukov, W Tierens et al.
- ICRF Heating Analysis on ASDEX Plasmas
Sanae-I. Ito, Kimitaka Itoh, Atsushi Fukuyama et al.

This content was downloaded from IP address 137.250.100.44 on 09/11/2026 at 14:52

OPEN ACCESS
IOP Publishing
Plasma Physics and Controlled Fusion
Plasma Phys. Control. Fusion **61** (2019) 125019 (20pp)
https://doi.org/10.1088/1361-6587/ab47a9

ICRF coupling in ASDEX upgrade magnetically perturbed 3D plasmas

G Suárez López[1,2], R Ochoukov[1], W Tierens[1], M Willensdorfer[1], H Zohm[1,2], D Aguiam[3], G Birkenmeier[1], V Bobkov[1], M Cavedon[1], M Dunne[1], H Faugel[1], R Fischer[1], H Fünfgelder[1], L Guimarãis[3], R McDermott[1], J-M Noterdaeme[1,4], E Seliunin[3], W Suttrop[1], the ASDEX Upgrade team[5] and the EUROfusion-MST1 team[6]

[1] Max Planck Institute for Plasma Physics, Boltzmannstraße 2, D-85748, Garching bei München, Germany
[2] Ludwig Maximilian University of Munich, Geschwister-Scholl-Platz 1, D-80539, München, Germany
[3] Instituto de Plasmas e Fusão Nuclear, Instituto Superior Técnico, Universidade de Lisboa, 1049-001 Lisboa, Portugal
[4] Applied Physics Department, University of Ghent, Sint-Pietersnieuwstraat 41, B-9000, Ghent, Belgium

E-mail: guillermo.suarez@ipp.mpg.de

Received 20 June 2019, revised 26 August 2019
Accepted for publication 25 September 2019
Published 11 November 2019

Abstract

The RF properties of the four ion cyclotron range of frequencies (ICRF) antennas in the ASDEX Upgrade tokamak are characterized in H-mode magnetically perturbed 3D discharges. An $n = 2$ magnetic perturbation (MP) field is applied and rigidly rotated, which allows diagnosing the separatrix displacement and consequent coupling change. We find the antenna loading resistance to be coherently modified by the resulting non-axisymmetric plasma equilibria, thus becoming a function of the applied MP field poloidal mode spectra. We perform a detailed statistical analysis, which correlates the change in loading resistance to the fast wave *R*-cutoff layer movements. From it, a 1D scaling is derived that differs from previous studies evaluated in pure axisymmetric plasma conditions. This experimentally derived scaling is used to predict the average loading resistance change of the ITER ICRF antenna under applied MPs. ICRF coupling simulations using measured 1D density profiles are performed with the RAPLICASOL code, in order to investigate the predictive capabilities of numerical state of the art tools. We find that both 1D conventional scaling laws and 1D numerical simulations fail to capture the 3D physics, and can substantially overestimate the measured loading resistance change up to a factor of ~3.

Keywords: ICRF, ASDEX Upgrade, MPs, coupling

(Some figures may appear in colour only in the online journal)

1. Introduction

Ion cyclotron range of frequencies (ICRF) systems are a widespread method for plasma heating and current drive used in experimental magnetic confinement fusion reactors. The common working principle relies on the excitation of the fast oscillatory mode of a magnetized plasma at a frequency matching the cyclotron frequency of a given ionic species in the plasma core, such that resonant damping can occur. The excitation is produced by an embedded antenna in the reactor wall, which contains a finite number of radiating straps, powered by a generator through a transmission line and

[5] See Meyer *et al* 2019 (https://doi.org/10.1088/1741-4326/ab18b8) for the ASDEX Upgrade team.
[6] See Labit *et al* 2019 (https://doi.org/10.1088/1741-4326/ab2211) for the EUROfusion-MST1 teams.

Original content from this work may be used under the terms of the Creative Commons Attribution 3.0 licence. Any further distribution of this work must maintain attribution to the author(s) and the title of the work, journal citation and DOI.

matching system. The fast wave, however, displays evanescence from where it is excited due to the low-density conditions at the plasma edge, and must reach the cutoff region before it starts propagating. This coupling process is equivalent to the optics phenomenon of frustrated total internal reflection, where the core plasma acts as the frustrating medium [1]. Therefore, the amount of ICRF power that can be coupled through the evanescent volume (rarer medium) at a given current amplitude in the antenna conductors is a function of the optical properties of this medium, determined by plasma density, composition, magnetic field, and the antenna parallel wavenumber ($k_\parallel$) spectrum. These variables thus determine the antenna radiation impedance Z_{rad} [2].

The dispersion relation that governs this phenomenon can be obtained from the cold plasma dielectric tensor formulation. For $\omega \ll \omega_{p,e}$, the electron plasma frequency, and in the limit of negligible electron mass $m_e \to 0$, we can express the dispersion relation in a simplified form that describes fairly well the fast wave evanescence and propagation properties [3, 4]:

$$n_\perp^2 = \frac{(R - n_\parallel^2)(L - n_\parallel^2)}{S - n_\parallel^2}, \tag{1}$$

where $n_\parallel = ck_\parallel/\omega$ is the parallel refractive index, c is the speed of light, ω is the angular frequency of the antenna, $n_\perp$ is the perpendicular refractive index, R, L and S are the Stix cold plasma dielectric tensor elements, which are functions of the plasma density, composition and magnetic field:

$$R = 1 - \sum_s \frac{\omega_{p,s}^2}{\omega(\omega + \Omega_s)} \tag{2a}$$

$$L = 1 - \sum_s \frac{\omega_{p,s}^2}{\omega(\omega - \Omega_s)} \tag{2b}$$

$$S = \frac{1}{2}(R + L) \tag{2c}$$

with $\omega_{p,s}^2 = n_s q_s^2 / \epsilon_0 m_s$ and $\Omega_s = q_s B/m_s$, the plasma frequency and the algebraic cyloctron frequency, where n_s is the density, q_s is the charge and m_s is the mass of the plasma species 's', and ϵ_0 is the vacuum permittivity. The dispersion relation in equation (1) displays two cutoffs, $n_\perp^2 = 0$, the R-cutoff ($n_\parallel^2 = R$) and the L-cutoff ($n_\parallel^2 = L$). The edge evanescent region is comprised by the volume between the antenna, where $n_\perp^2 < 0$, and the R-cutoff, where the wave becomes propagative towards the plasma core.

Maximization of the radiated power requires increasing either $\mathrm{Re}(Z_{\mathrm{rad}})$ or the current amplitude in the straps. The latter is limited by engineering constraints due to voltage stand-off [5]. The former depends on the evanescence conditions in front of the ICRF antenna, approximated by equation (1). Changes in the plasma kinetic profiles or magnetic field within the coupling region translate into changes of Z_{rad}, and thus, changes of the radiated power for a given current amplitude in the antenna conductors. The dependence of Z_{rad} on plasma parameters has been extensively studied assuming the evanescent medium to be one-dimensional, with gradients in the kinetic profiles and magnetic field only in the normal direction to the ICRF antenna [2, 6]. The additional inclusion of poloidal asymmetries proved to be important in understanding the changes in coupling performance when the plasma triangularity is experimentally scanned [7]. Recently, special attention has been dedicated to the understanding of the effect of 3D density configurations due to the interest in improved antenna coupling capabilities with gas puffing techniques [8, 9]. Integration of ICRF systems in stellarators [10], and the understanding of ICRF coupling physics in arbitrary 3D geometries, extends this interest to 3D kinetic profiles and 3D magnetic fields. In tokamaks, this latter case is present when plasma instabilities arise, such as MHD modes, or when magnetic perturbation (MP) in-vessel coils are applied for edge-localized mode (ELM) mitigation and suppression. The response of the ICRF system to MPs is also of special interest to ITER, which counts on an MP coil set for ELM control [11] and an ICRF system expected to deliver 20 MW of heating power [12, 13]. So far, however, the effect of non-axisymmetric plasma configurations has been neglected in the design of the ITER antenna, and their impact is mostly unknown. In ASDEX Upgrade, dedicated experiments to understand the interplay between MPs and ICRF heating had been carried out so far with static MP fields, which can only account for the effect of the toroidally localized plasma asymmetries on the ICRF antennas [14, 15]. No effect of the applied poloidal phasing, defined as the differential phase between the current waveforms of the upper and lower toroidal rows of MP coils in ASDEX Upgrade, $\Delta\varphi_{\mathrm{UL}}$, on the ICRF coupling was found. A more recent study using rotating MP fields, however, revealed that ICRF coupling can be coherently affected by the induced non-axisymmetric plasma structure produced by different MP configurations [16]. This observation, conjugated with the reduced availability of data for ICRF heated MP discharges, motivated a dedicated set of experiments. Therefore, in this paper, we have systematically studied for the first time the coupling properties of the fast wave when MP fields are applied and rigidly rotated. This allows us to assess the impact of plasma non-axisymmetric profiles, regardless of where the ICRF antennas are placed inside the vessel. For this purpose, we have utilized the MP and ICRF systems in the ASDEX Upgrade tokamak. In addition, the poloidal phasing of the MP coils is scanned, and the effect of the plasma response to the MPs on the ICRF system is discussed. It is shown that for the studied plasma conditions, $\Delta\varphi_{\mathrm{UL}}$ plays a significant role on the response of the ICRF system.

The paper is organized as follows: in section 2 the experimental setup is introduced. Plasma discharges with ICRF heating and MPs are described along with measurements of key RF quantities. The effect of different MP phasings on ICRF coupling is studied. In section 3, we compare the experimental results against 1D analytical formulas and experimentally-derived scalings found in the literature, in order to assess their validity under our experimental conditions. A statistical analysis of the data allows deriving a 1D scaling for the average loading resistance change under applied MPs. In section 4, numerical simulations are presented and compared to the experiments. In

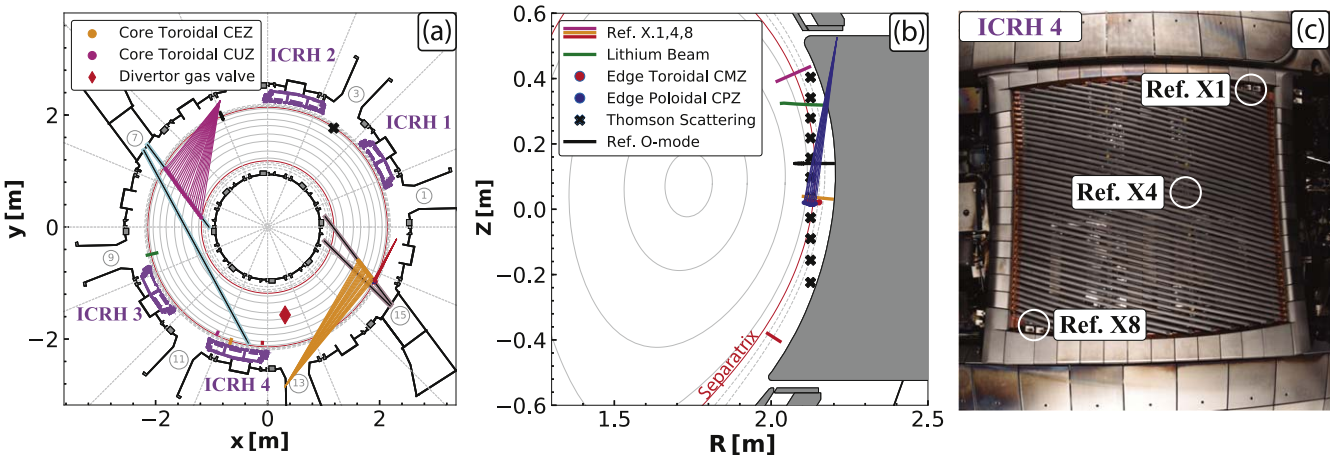

Figure 1. (a) ASDEX Upgrade toroidal cross section with toroidal view of employed diagnostics, divertor gas valve and ICRF antennas. (b) ASDEX Upgrade poloidal cross section with poloidal view of employed diagnostics: ICRF embedded reflectometry (Ref. X, see (c)), lithium beam, CXRS, Thomson scattering and O-mode reflectometry. (c) In-vessel picture of ICRH4 with positions of embedded reflectometry.

section 5, the experimentally-derived 1D scaling of section 3 is utilized to predict the average loading resistance changes in the ITER ICRF antenna due to MP plasma displacements. In section 6, we present the conclusions of this study.

2. Experimental setup and results

2.1. ICRF system and measurements

Four ICRF antennas are in current use on ASDEX Upgrade: a pair of 2-strap antennas using boron-coated limiters (ICRH1 and ICRH3) and a pair of 3-strap antennas using tungsten coated limiters (ICRH2 and ICRH4, see figure 1(a)). Both 2-strap antennas are fed jointly from two RF generators connected together by a combiner-splitter system [7]. Each antenna is then individually matched by two stub tuners and a T-Junction that splits the power to each strap. The 3-strap antennas are also fed by two RF generators, such that one generator feeds the central strap of both antennas and the other one feeds the side straps. This is done to allow for different power balances and phasing between the outer straps and the inner strap of each antenna, in order to reduce the net RF image currents on the antenna limiters [19]. Each transmission line feeding a central strap as well as the ones that feed the side straps are matched with two stub tuners. In order to diagnose the change in ICRF coupling, measurements of the loading resistance, R_L, are taken. The loading resistance gives a good estimate of the degree of matching between the transmission line-strap system and the plasma. Its measurement is performed by a directional coupler placed behind the generator-side stub tuner and a voltage probe located at the voltage antinode in the unmatched antenna-side transmission line, such that:

$$R_L = \frac{2Z_0^2 P_{\text{coupled}}}{V_{\text{max}}^2}, \tag{3}$$

where P_{coupled}, V_{max} and $Z_0 = 25\ \Omega$ are the power coupled to, the maximum voltage in, and the characteristic impedance of the unmatched transmission line. Due to the feeding arrangement in ASDEX Upgrade, measurements of the loading resistance are available for each individual transmission line—strap system, except in the case of the 3-strap antennas, for which a single measurement is present for both side straps together and another one for each central strap. The reader is referred to [20] for a detailed description of the ASDEX Upgrade ICRF antenna feeding arrangement.

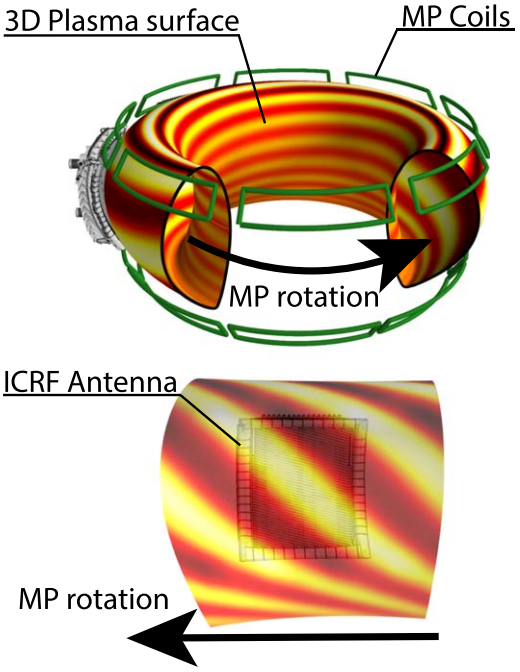

Figure 2. Arbitrary $n = 2$ deformed LCFS computed by the VMEC code [17, 18], used to demonstrate the possible 3D plasma deformation seen by the ICRF antennas.

2.2. Discharges description

ELM control requires the MP field to be applied with a specific poloidal mode spectrum which is amplified the most by ideal MHD modes excited in the plasma edge. These

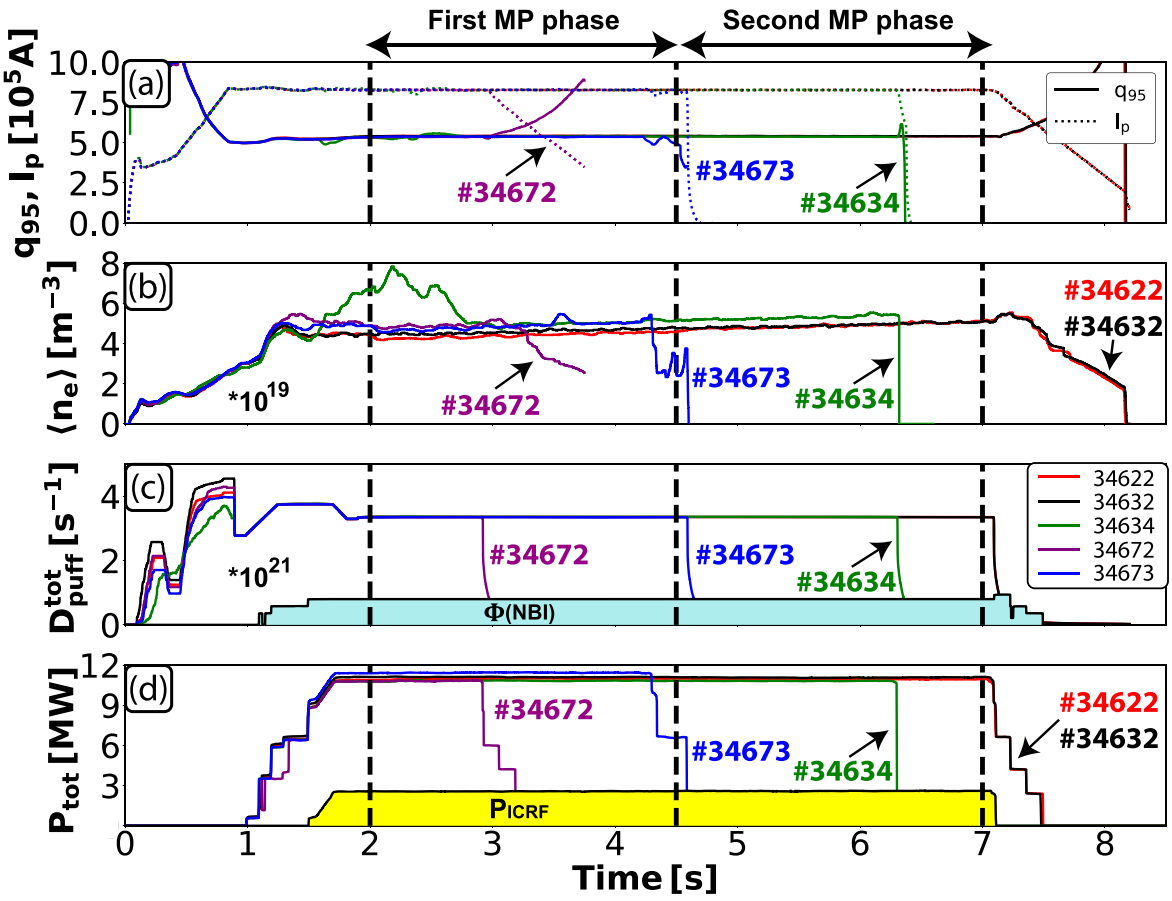

Figure 3. Time traces of the considered discharges: (a) safety factor at 95% poloidal flux, q_{95}, and plasma current, I_p (b) line-averaged electron density $\langle n_e \rangle$, (c) total deuterium fueling D^{tot}_{puff} with NBI contributed particle flux and (d) total power P_{tot} out of which, ICRF power fraction, P_{ICRF}.

modes create a field-aligned plasma displacement which has been well predicted and characterized in many tokamaks, such as ASDEX Upgrade [21, 22], DIII-D [23] and MAST [24]. The induced 3D plasma displacement creates a non-axisymmetric density profile that extends into the ICRF fast wave coupling region in the scrape-off layer (SOL). The degree of displacement and its topology depend upon the toroidal and poloidal mode number spectrum of the MP field, the edge plasma current and the edge pressure gradient. On ASDEX Upgrade, two toroidally distributed, poloidally spaced rings of 8 MP coils each, are installed as depicted in figure 2. It is then possible to modify the MP applied poloidal mode spectrum by varying the differential phase of the coil current waveforms in the two rings, termed $\Delta\varphi_{UL}$ here.

A set of five H-mode discharges was performed in order to study the effect of MPs on ICRF coupling. In order to explore a reactor-relevant scenario, two main parameters were optimized: high plasma $\beta_N \sim 2$ and low electron and ion pedestal collisionalities $\nu_e^* \sim 0.25 - 0.65$, $\nu_i^* \sim 0.15 - 0.25$. Time traces for the edge safety factor q_{95}, plasma current I_p, line-averaged electron density $\langle n_e \rangle$, deuterium puff D^{tot}_{puff} and applied total power P_{tot} can be seen in figure 3. The discharges were performed in Lower Single Null configuration, with the ion $\vec{\nabla}B$ drift pointing towards the X-point. The plasma parameters were kept constant with on-axis $|B_t| = 2.5$ T, $I_p = 0.8$ MA, resulting in an edge safety factor $q_{95} \sim 5.3$, with central line-averaged electron density $\langle n_e \rangle \sim 5 \times 10^{19}$ m^{-3}. A total heating power of $P_{tot} \sim 11.5$ MW was applied, out of which $P_{ICRF} \sim 2.2$ MW was delivered simultaneously by the four ICRF antennas in dipole phasing. This value is the generator power after subtracting the dissipated power in the 3 dB hybrid coupler loads and the Ohmic losses in the transmission lines, accounted for by vacuum measurements on the 2-strap antennas. The ICRF heating scenario was minority (*H*)-*D*, second harmonic *D* ($\omega_{ICRF} = 2\omega_{c,D}$), with central deposition at a frequency $\nu_{ICRF} = 36.5$ MHz. The rest of the heating power was supplied by NBI (~6.8 MW) and ECRH (~2.5 MW). The discharges were fueled with deuterium gas by a single lower divertor valve located in sector 13 (figure 1(a)). One of the discharges was performed as a reference (#34632), without MPs. For the rest of discharges the MPs were switched on at 2 s, during the flat top, and were supplied with $I_{coil} = 5$ kA × turns. Two differential phasings, $\Delta\varphi_{UL}$, were applied per discharge in $n = 2$ toroidally symmetric configuration and rigidly rotated with a frequency of $\nu_0 = 3$ Hz for diagnostic purposes. The last two discharges terminated prematurely due to disruptions, and only one $\Delta\varphi_{UL}$ phase was acquired for them, resulting in a set with $\Delta\varphi_{UL} = \{-145°, -45°, 0°, +45°, +90°, 180°\}$. For the

Table 1. Discharge numbers with MP configuration and average parameters of interest: number of used MP periods in the analysis, time-averaged poloidal plasma beta $\langle\beta_{\rm pol}\rangle_t$, time-averaged effective charge number $\langle Z_{\rm eff}\rangle_t$, time-averaged electron/ion collisionality at the pedestal top $\langle\ \nu_{\rm e}^*\rangle_t/\langle\ \nu_{\rm i}^*\rangle_t(\rho_{\rm pol}=0.9)$.

Shot #	$\Delta\varphi_{\rm UL}$	# used MP periods	$\langle\beta_{\rm pol}\rangle_t$	$\langle Z_{\rm eff}\rangle_t$	$\langle\ \nu_{\rm e}^*(\rho_{\rm pol}=0.9)\rangle_t$	$\langle\ \nu_{\rm i}^*(\rho_{\rm pol}=0.9)\rangle_t$
34622	0°, 180°	8, 8	1.38, 1.37	1.42, 1.41	0.44, 0.64	0.18, 0.24
34632	No MPs	—	1.42	1.37	0.57	0.19
34634	−45°, 45°	5, 5	1.53, 1.47	1.57, 1.33	0.25, 0.25	0.16, 0.16
34672	90°	3	1.5	1.30	0.30	0.15
34673	−145°	4	1.52	1.28	0.29	0.15

discharge with $\Delta\varphi_{\rm UL}=\{-45°, +45°\}$ a sputtered tungsten flake produced a density increase from 1.5 to 3 s, hence this time slice is rejected in the analysis. The resulting average plasma beta poloidal, $\langle\beta_{\rm pol}\rangle_t$, electron and ion collisionalities, $\langle\nu_e^*\rangle_t$, $\langle\nu_i^*\rangle_t$, are presented in table 1 for reference. The collisionalities were computed according to the formulas included in [25, 26] using the electron density and temperature profiles obtained from the integrated data analysis [27] and the ion temperature profiles obtained from charge exchange recombination spectroscopy (CXRS). All the profiles are evaluated at $\rho_{\rm pol}=0.9$, i.e. at the pedestal top. The $Z_{\rm eff}$ value was obtained from Bremsstrahlung emission. For the ion density, a fractional boron impurity percentage of $n_{\rm B}/n_e\sim 0.005$ was consistently computed by the CHICA code [28]. In order to represent all the impurity species, this value was scaled to match the measured $Z_{\rm eff}$, such that $(n_{\rm B}/n_e)_{\rm scaled}\sim 0.013-0.03$. Due to the passive stabilization loop (PSL) on which the MP coils are mounted inside the vessel, the applied perturbation field is attenuated and lagged with respect to the expected one when no conducting structures are taken into account. The combination of this attenuation and a pedestal pressure of $p_{\rm ped}\sim$ 16.5 kPa ($p_{\rm ped,e}\sim 7.5$ kPa), results in the ELM behavior to be unchanged by the MPs, that is, the discharges behaved as regular ELMy H-modes. This behavior is consistent with previous studies of ELM mitigation and suppression accessibility in ASDEX Upgrade [29].

Even though all discharges were performed with the same input waveforms on the actuators, some differences are noticeable. Discharges #34622 and #34632 have higher electron collisionalities than the others, which arise from lower pedestal electron temperatures. They were performed on the same experimental session and thus with very similar machine conditioning. On the other hand, the rest of discharges were distributed into two different experimental sessions, and the difference in plasma parameters is attributed to different machine conditioning and core MHD activity. Furthermore, since no feedback control was used on the density profile, the average value is seen to increase during the discharge time for all the performed experiments, due to NBI fueling and the forward gas puff. While electron density changes have an impact both on the plasma response to the MPs and on the ICRF coupling, such changes are taken into account for all the studied quantities, as discussed in section 2.5, through baseline correction and sinusoidal fits representing the average value over the considered MP periods.

2.3. Plasma response to applied MPs. Effect of MPs on the SOL density profiles

The plasma edge 3D displacement was evaluated with toroidally localized diagnostics in the same fashion as in [21, 22]. The MP field is rigidly rotated and the diagnostics register variations in the plasma kinetic profiles locked to the external field as a time-dependent oscillation of their measurement quantity. In this study, we have used the lithium beam diagnostic [30], two chords of the CXRS diagnostic (termed CMZ: edge toroidal CXRS and CPZ: edge poloidal CXRS) [31], three X-mode reflectometry channels embedded in the 3-strap antenna ICRH4 [32], labeled as Ref. X{1,4,8} in figure 1, and the midplane O-mode reflectometer [33]. These diagnostics are positioned on the low-field side (LFS) of ASDEX Upgrade, with the CXRS chords, Ref. X4 and Ref. O-mode at the outboard midplane (OMP), here $\theta\approx 0$, the lithium beam and Ref. X1 above the midplane and Ref. X8 below the midplane. The CXRS diagnostics track the B^{5+} impurity line intensity corresponding to $\lambda\approx 494$ nm, which is taken as a proxy for the B^{5+} impurity density, while in the lithium beam and reflectometers case we use the reconstructed electron density profiles. The plasma displacements are evaluated in time-domain by tracing the position ($d_{\rm LOS}^{\rm iso}$) of constant intensity or density layers over the line of sight (LOS) of each diagnostic during the MP rotation. The data is ELM-filtered, and an ordinary least square (OLS) fit is performed to the position of these iso-layers. The OLS fit computes the estimators for the amplitudes of sine functions ($|\xi_n(\nu_j)|$) with up to 4 harmonics of the fundamental frequency, ν_0, i.e. $\nu_j=(j+1)\nu_0\ \forall j\in[0,3]$, and the coefficients of a cubic polynomial (α_k) for baseline subtraction, such that:

$$d_{\rm LOS}^{\rm iso}\approx\sum_{j=0}^{j=3}|\xi_n(\nu_j)|\sin(\omega_j t+\phi_j)+\sum_{k=0}^{k=3}\alpha_k t^k, \qquad (4)$$

where $\omega_j=2\pi\nu_j$ and ϕ_j is the phase of each sine function. The resulting displacement profiles of the density layers for $|\xi_n(\nu_0)|$ can be seen in figure 4 for the $\Delta\varphi_{\rm UL}=0°$ and reference cases. During the MP phases, the plasma displacements decay monotonically in the SOL. This is well-registered by both the lithium beam and the reflectometers, with the exception of a 'bump' observed in the lithium beam at around $n_e\sim 7-8\times 10^{18}\,{\rm m}^{-3}$, which matches the position of the H-mode density shoulder [34]. Very good agreement is found among all the diagnostics in the region

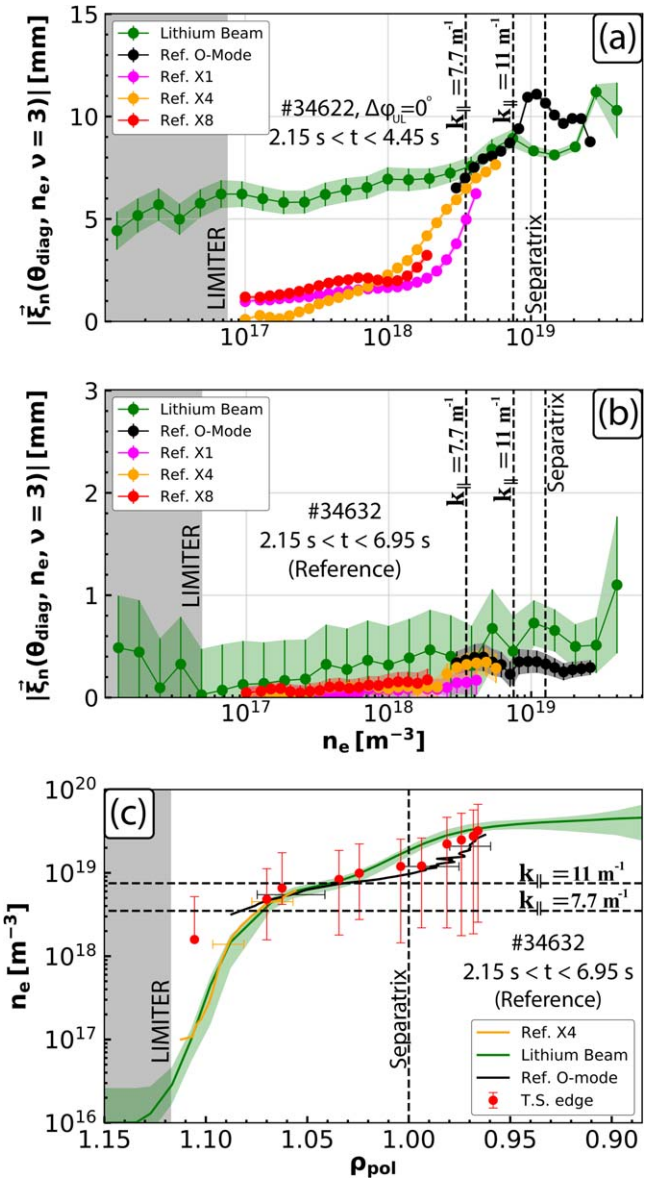

Figure 4. (a), (b) n_e-dependence of the OLS $|\xi_n(\nu_0)|$ estimator amplitude for the $\Delta\varphi_{\rm UL} = 0°$ and reference cases. The time-averaged n_e at the limiter was evaluated using the lithium beam LOS on a per-discharge basis (c) Time-averaged n_e profiles for the reference case from Ref. X4, Ref. O-mode, lithium beam and edge Thomson scattering diagnostics. Reflectometry error bars are taken as 1σ and only displayed for some points.

$3 \times 10^{18}\,\mathrm{m}^{-3} < n_e < 8 \times 10^{18}\,\mathrm{m}^{-3}$, which includes the R-cutoff for all the ICRF antennas. However, in the far SOL no absolute agreement is found when MPs are active, despite the fact that the fluctuation level for ν_0 is very similar when no MPs are applied. The ICRF limiter position in density-space is included along the lithium beam LOS, to give a reference of the measurements alignment and discard its effect on the displacements. The time-averaged density profiles are also included for the reference case as a function of the $\rho_{\rm pol} = \sqrt{\chi - \chi_0/\chi_{\rm sep} - \chi_0}$ magnetic coordinate, with χ the poloidal flux at a given point, $\chi_{\rm sep}$ the poloidal flux at the separatrix and χ_0 the poloidal flux at the magnetic axis. This comparison highlights the good agreement of the diagnostics in axisymmetry in the $n_e \sim 10^{18}\,\mathrm{m}^{-3}$ region. Measurements of the density profile in reflectometry depend on different parameters: X-mode reflectometry requires an accurate magnetic equilibrium reconstruction in order to correctly place the position of the first fringe, or first plasma *echo* [35]. The precision of the magnetic reconstruction is hampered when MPs are applied, since the used tool (the CLISTE code [36]), is a Grad–Shafranov solver that can only handle axisymmetric plasmas. Furthermore, there are built-in assumptions when computing the density profiles, such as a constant residual density for the wave upper cut-off determination, that can affect the density profile initialization [37]. Similarly, in O-mode reflectometry while the magnetic field plays no role, the assumption of a constant value for the $R(n_e = 0) = 2.24$ m is used. On the other hand, the profiles should be less sensitive to these effects the farther they are from their initialization point, which can explain the good agreement with the lithium beam at the $n_e \sim 10^{18}\,\mathrm{m}^{-3}$ density layers. A detailed study of the differences between the diagnostics and possible improvements to X-mode reflectometry when a proper 3D magnetic reconstruction is used, goes however, beyond the scope of this paper. It should also be kept in mind that the lithium beam profiles become more inaccurate inside the pedestal region, $n_e \gtrsim 3 - 4 \times 10^{19}\,\mathrm{m}^{-3}$, where beam attenuation can play an important role [30]. In this study, we have included the data obtained from reflectometry under the premises that:

1. Reflectometry profiles are always used in relative terms, that is, to compare the changes between the minimum and maximum plasma-antenna gap distances. In this manner, systematic errors play a smaller role.
2. The good agreement among all the diagnostics in the $n_e \sim 10^{18}\,\mathrm{m}^{-3}$ density layers further motivates their validity in this region. For the ICRF cutoff oscillation, either using the lithium beam or reflectometry density profiles does not change the conclusions of our study. The R-cutoff displacements are nearly equivalent for both diagnostics (we refer to figure 4(a)).
3. The ICRH4 embedded X-mode reflectometers offer a description of the poloidal distribution of the density profile. This information is very valuable to the study at hand, and unavailable otherwise.

From now on, we will focus exclusively on three positions of interest for this study: the separatrix and the two main R-cutoffs for the 2-strap and 3-strap antennas. The iso-density and iso-intensity values for the separatrix are taken to be a time-average of all MP periods in a given $\Delta\varphi_{\rm UL}$ of the $\rho_{\rm pol} = 1$ value, as determined by CLISTE, and were found to be $n_e^{\rm iso} \approx 1.2 \times 10^{19}\,\mathrm{m}^{-3}$, $I_{\rm CXRS}^{\rm iso} \approx 2 \times 10^{16}\,\mathrm{ph/(m^2 \times sr \times s)}$. The lithium beam measurements are corrected for the geometrical angle between the diagnostic LOS and the normal vector to the axisymmetric CLISTE flux surface, such that a correct normal displacement, $\vec{\xi}_n$, can be obtained. This results in displacements about ~6% smaller than those measured by the diagnostic. The R-cutoff positions are obtained from equation (1) with the assumption of a *H–D* mixture of 5%–95% in the plasma, and

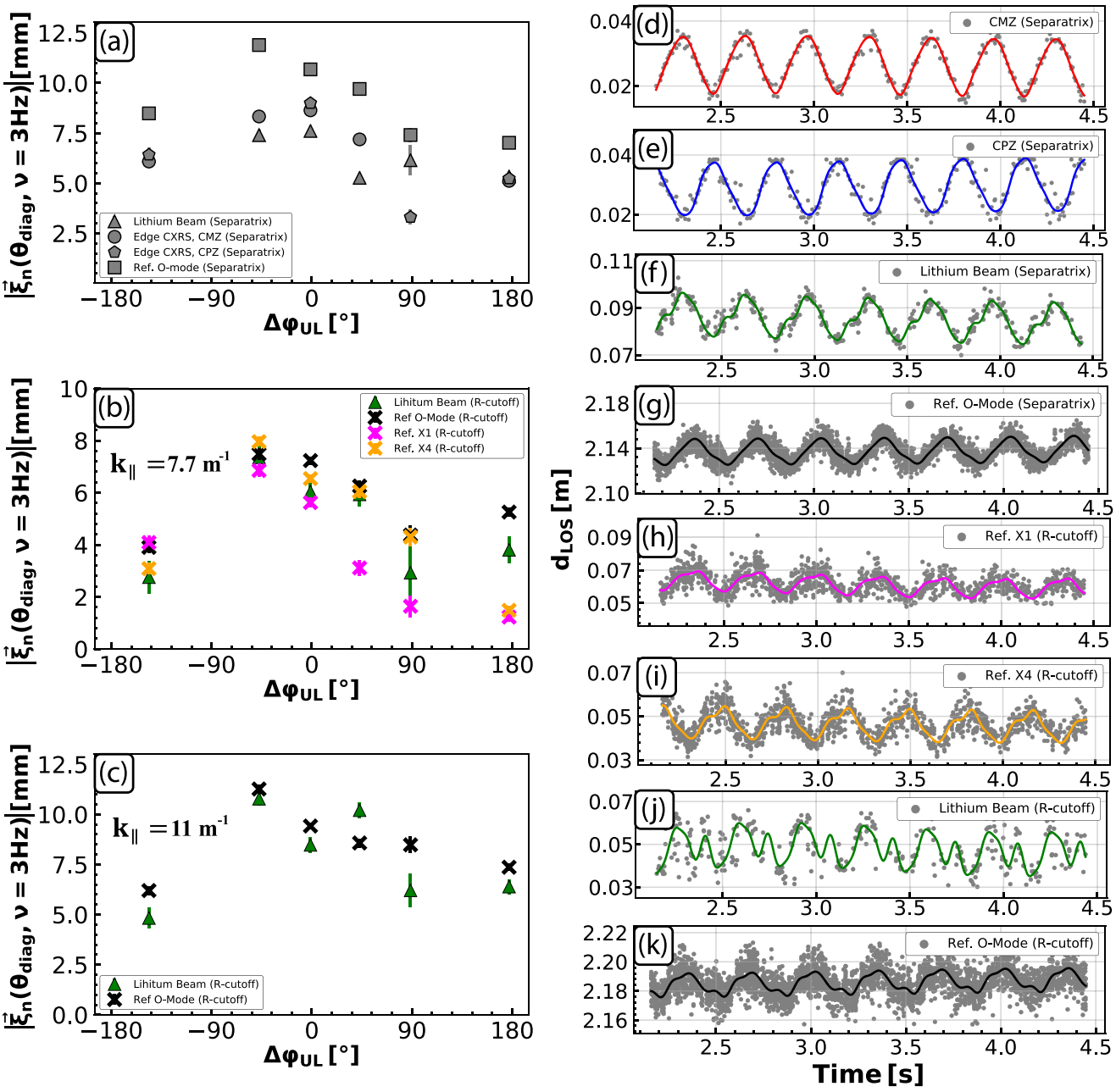

Figure 5. (a) Plasma normal displacements $|\xi_n(\nu_0)|$ measured at the separatrix by the lithium beam, two CXRS diagnostics and O-mode reflectometry. (b) Plasma normal displacements at the *R*-cutoff ($k_\parallel = 7.7\ \mathrm{m}^{-1}$) measured by the lithium beam, X-mode reflectometers 1 and 4, and O-mode reflectometry, (c) Plasma normal displacements at the *R*-cutoff ($k_\parallel = 11\ \mathrm{m}^{-1}$) measured by the lithium beam and O-mode reflectometry. (d), (e) CMZ and CPZ separatrix iso-intensity layer position time trace, (f) lithium beam separatrix iso-density layer position time trace, (g) O-mode reflectometry separatrix iso-density layer position time trace, (h), (i) Ref. X1 and X4 *R*-cutoff layer ($k_\parallel = 7.7\ \mathrm{m}^{-1}$) position time trace, (j) lithium beam *R*-cutoff layer ($k_\parallel = 7.7\ \mathrm{m}^{-1}$) position time trace, (k) O-mode reflectometry *R*-cutoff layer ($k_\parallel = 7.7\ \mathrm{m}^{-1}$) position time trace. The positions, d_{LOS}, of the time traces in (d)–(k) correspond to each diagnostic LOS for the $\Delta\varphi_{\mathrm{UL}} = 0°$ case, and the solid lines are OLS fits.

using the CLISTE axisymmetric magnetic induction field calculation. This way, the total tokamak field is included in the analysis, although, partially inaccurate due to the assumption of pure axisymmetry. For the $k_\parallel$ values, we will take those for which the predicted Fourier spectra of the field-aligned RF magnetic field component by plasma loaded numerical calculations finds a maximum close to the antenna Faraday screen (FS). For the 3-strap antennas, a value of $k_\parallel = 11\ \mathrm{m}^{-1}$ ($n_\parallel \sim 14.4$ for the used ν_{ICRF}) is usually representative for dipole phasing, as the power balance between the central and outer straps was kept at 1.5:1 [20]. The resulting *R*-cutoff density is of the order of $n_e^{\mathrm{cutoff}} \sim 7.5 \times 10^{18}\ \mathrm{m}^{-3}$, which is positioned beyond the X-mode reflectometry density measurements, hence, only the

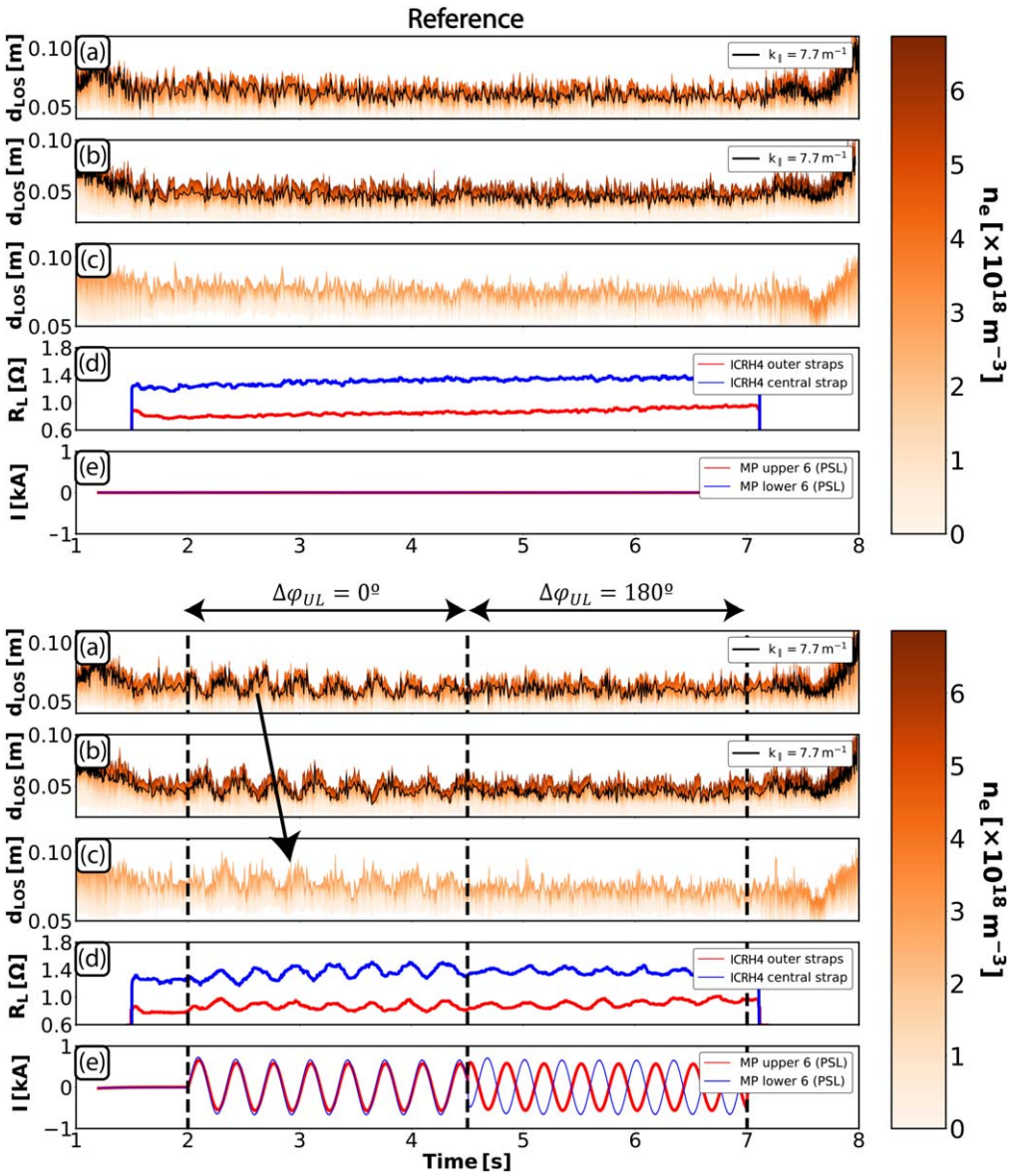

Figure 6. Upper plot: Reference discharge with no MPs. Lower plot: discharge with $\Delta\varphi_{\rm UL} = \{0°, 180°\}$. (a)–(c) Density measurements at the different reflectometer channels Ref. X1, Ref. X4, Ref. X8 plotted along lines of sight distance, $d_{\rm LOS}$. The tilted arrow marks the direction of propagation of the density perturbation. (d) Loading resistance measured at the feeders of ICRH4. A sliding median filter has been applied for display purposes. (e) Applied currents to the MPs, corrected for the PSL attenuation.

lithium beam and O-mode reflectometry diagnostics will be used for the analysis of the 3-strap antennas. On the other hand, the main parallel wavenumber of the 2-strap antennas spectrum, $k_\parallel = 7.7\ {\rm m}^{-1}$ ($n_\parallel \sim 10$) [20, 38] results in a lower R-cutoff density of the order of $n_e^{\rm cutoff} \sim 3.5 \times 10^{18}\ {\rm m}^{-3}$, that is well-resolved by X-mode reflectometry measurements, and thus are also included in the analysis. The $|\xi_n(\nu_0)|$ fit amplitudes as a function of the MP phasing, and the time traces for $\Delta\varphi_{\rm UL} = 0°$ can be seen in figure 5. It is to be noted that the abscissa values in (a)–(c) are slightly different from the ones presented in table 1. The PSL model from [39] has been incorporated into the calculations, which results in slightly different $\Delta\varphi_{\rm UL}$ values from the ones applied to the coil current waveforms of the order of ∼3°.

From the measurements, it is clear that $|\xi_n(\nu_0)|$ depends on the applied $\Delta\varphi_{\rm UL}$, not only for the separatrix, but also for the ICRF R-cutoffs. The maximum separatrix displacements are seen around $-90° < \Delta\varphi_{\rm UL} < 0°$ while the minimum displacements lie somewhere between $90° \leqslant \Delta\varphi_{\rm UL} \leqslant 180°$. In general, very good agreement is found at the separatrix between the CXRS diagnostics and the lithium beam, even though they sit at different poloidal positions. The biggest scatter in the data is seen for the $\Delta\varphi_{\rm UL} = 90°$ case, which has the least number of MP periods available, and thus the poorest statistics, also resulting in larger measurement error bars. On the other hand, the O-mode reflectometer tends to over-estimate the displacements in this region. In the SOL, the reflectometers and the lithium beam measure the same

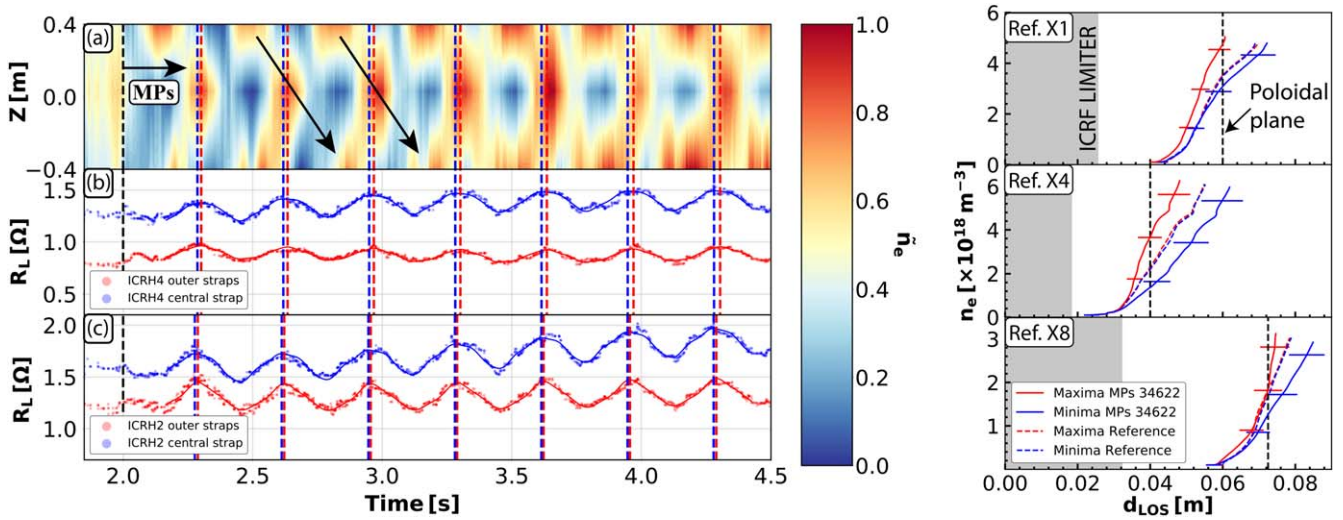

Figure 7. Left: (a) Density contour from Ref. X1, Ref. X4 and Ref. X8 as intersected by a poloidal plane with distance to the reflectometer horn antennas of $d_{\mathrm{ref.X1}} = 6$ cm, $d_{\mathrm{ref.X4}} = 4$ cm and $d_{\mathrm{ref.X8}} = 7.25$ cm. The tilted arrows mark the direction of rotation of the kink displacement along the antenna. (b) loading resistance time traces of ICRH4 with local maxima, (c) loading resistance time traces of ICRH2 with local maxima. Right: 1D density profiles from Ref. X1, Ref. X4 and Ref. X8 at maximum and minimum approach to ICRH4. The profiles from discharge #34622 with MPs are included as solid lines, while the profiles from #34632 without MPs are included as dashed lines.

monotonic dependence of the *R*-cutoffs' displacement on the applied $\Delta\varphi_{\mathrm{UL}}$. Once again, fair agreement is found between the lithium beam and the midplane measurements from Ref. X4. and Ref. O-mode, even though they are positioned at different poloidal locations on the LFS. It is interesting to observe that the separatrix $|\xi_n(\nu_0)|$ dependence on $\Delta\varphi_{\mathrm{UL}}$ differs slightly from that of the *R*-cutoffs. The density profile in the SOL can be locally affected by fueling and recycling processes due to plasma-wall interactions, as well as by ICRF induced density perturbations. In the case of discharge #34634, the early detachment of a tungsten flake is seen to increase the SOL density throughout the discharge. Therefore, these differences suggest that SOL physics and machine conditioning also play a role in the amplitude of the edge plasma displacements. Knowledge of the plasma response to the MPs becomes in this case not enough to predict which $\Delta\varphi_{\mathrm{UL}}$ phasings will have the biggest impact on ICRF coupling. Finally, while the complete non-axisymmetric structure will dictate the behavior of the ICRF antenna, the SOL trend already hints to which phasings might have the biggest impact on the ICRF coupling. A detailed study of the measured loading resistance is presented in the next sections.

2.4. Impact of perturbed SOL density profiles on ICRF coupling performance

X-mode reflectometry density profiles and loading resistance measurements are presented in figure 6 for the $\Delta\varphi_{\mathrm{UL}} = \{0°, 180°\}$ cases and the reference discharge. All considered time traces were analyzed with ELM-filtered data. The density profiles are plotted along the LOS coordinate of the X-mode reflectometer channels d_{LOS}, where $d_{\mathrm{LOS}} = 0$ represents the reflectometer horn antenna position. Since the reflectometer uses X-mode, the maximum resolvable density differs among channels depending on their radial location inside the vessel. A clear density oscillation is observed in front of ICRH4 when the MPs are rotated. The *R*-cutoff position (included in the figure is the one for the 2-strap antennas) oscillates with the density profile, and the amplitude of the oscillation directly depends on the $k_{\parallel}$ value, as it was observed in figure 4. Coherent loading resistance oscillations are registered, as measured in the two feeding lines of the same antenna. It is worth noting that when the MPs change from in-phase ($\Delta\varphi_{\mathrm{UL}} = 0°$) to out of phase ($\Delta\varphi_{\mathrm{UL}} = 180°$), the plasma response changes, decreasing the displacements in front of the antenna and thus the coupling oscillations. It is also seen that the loading resistance oscillations follow closely the density perturbation on Ref. X4, which is the reflectometer channel best aligned with the geometrical center of ICRH4. A more comprehensive way of plotting the density perturbation versus the loading change can be found in figure 7. There, we plot the density structure arising from the intersection of a poloidal plane with the three X-mode reflectometer channels. Since the gap between the ICRF antenna and the plasma changes poloidally, the distance between the ICRF antenna and the plane is also made to change accordingly. Three separation values are chosen for each reflectometer, $d_{\mathrm{ref.X1}} = 6$ cm, $d_{\mathrm{ref.X4}} = 4$ cm and $d_{\mathrm{ref.X8}} = 7.25$ cm. A mapping function for the density has been used such that the oscillation can be commonly observed using the same normalized scale:

$$\tilde{n}_e^j = \frac{n_e^j - \min(n_e^j)}{\max(n_e^j) - \min(n_e^j)} \in [0, 1] \tag{5}$$

with $j = 1, 4, 8$. The toroidal mode structure of the perturbation can be well resolved due to the high-enough sampling frequency of the reflectometers during the MP rigid rotation. On the other hand, the poloidal mode structure is poorly resolved, since only three measuring positions cover approximately 0.8 m of vertical distance. Nevertheless, the 3D density structure can be seen traveling the antenna from top to bottom, as marked by the tilted

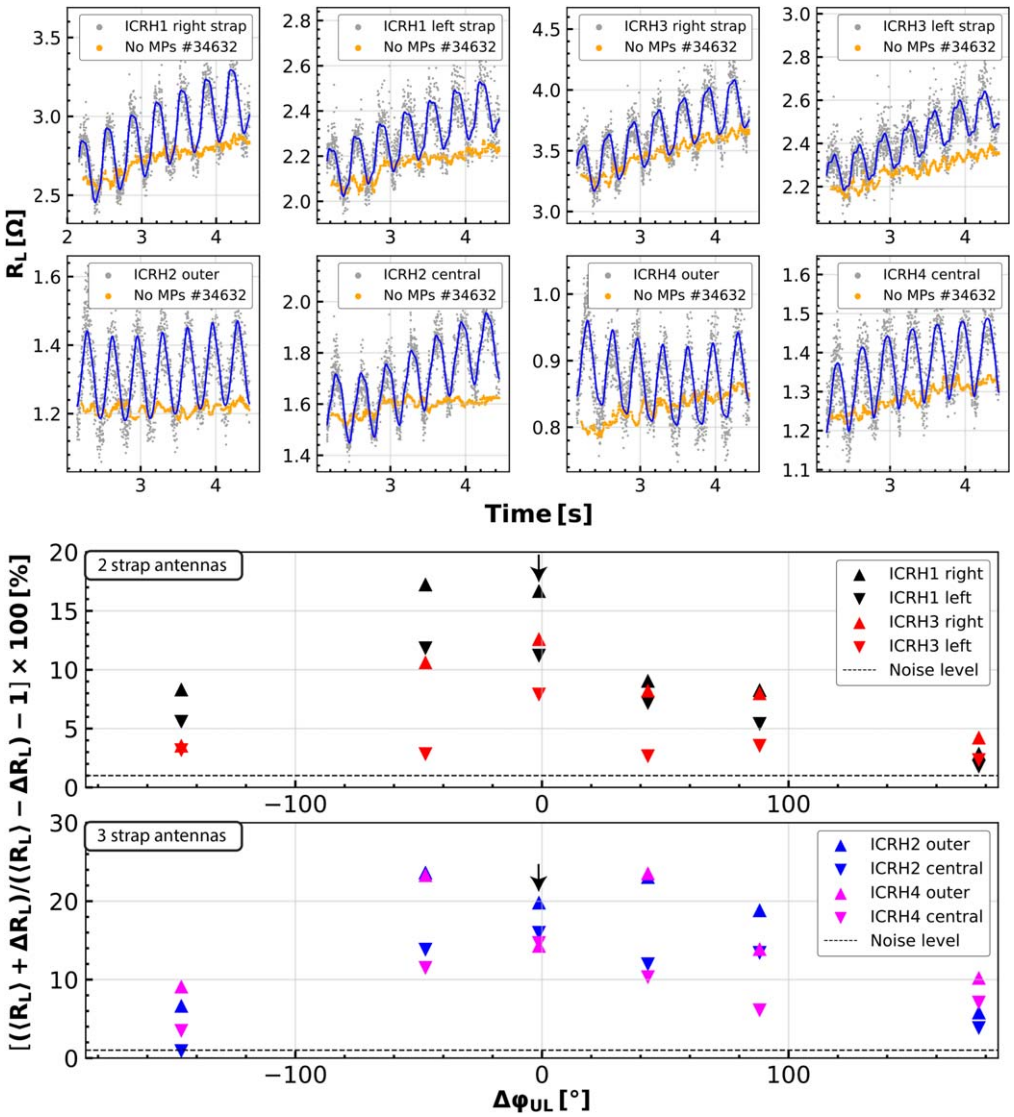

Figure 8. Upper plots: loading resistance of each ICRF antenna feeder and OLS fit for the case of $\Delta\varphi_{\mathrm{UL}} = 0°$ (blue), and reference with no MPs (orange). A sliding median filter with a 51 point window has been applied to the reference case for display purposes. Lower plot: loading resistance percentage change for the (upper) 2-strap antennas and (lower) 3-strap antennas. Left and right straps from the 2-strap antennas, as seen from the antenna reference frame towards the plasma. Outer straps in each 3-strap antenna are connected to the same feeder. The arrow marks the $\Delta\varphi_{\mathrm{UL}} = 0°$ amplitudes of the shown loading resistance time traces in the upper plot. The marker size is representative of the OLS 1σ uncertainty.

arrows. The antenna loading resistances have been fitted with an OLS fit, in the same fashion as indicated before, in order to obtain the times when the local maxima happen (dashed red and blue lines in figure 7). These lines for ICRH4 have been extended upwards to the density plot for comparison. The maxima are well correlated with the density perturbation when it is closer to the antenna center. We hypothesize that this is due to the ballooned structure of the perturbation on the LFS of the tokamak, thus covering a larger portion of the ICRF antenna the closer it is to its center. On the right, one-dimensional density profiles are plotted for the three reflectometer channels, representative of local maximum and minimum approach to the ICRF antenna position when the MP phasing was set to $\Delta\varphi_{\mathrm{UL}} = 0°$. The profiles were calculated by performing local averages centered at each extrema over 50 ms windows. Each local averaged profile is then averaged again together for all the maxima and minima separately. The density profiles for the reference discharge with no MPs are evaluated in the same way, and included as dashed lines. Error bars are added for some points as one standard deviation of the profiles. Significant displacements of the density profiles are seen close to the ICRF antenna in the MP case, while for the reference case the profiles have a steady position. In the next section, we will investigate how the different MP phasings affect the ICRF antennas loading resistance.

2.5. Loading resistance change as a function of applied MP phasing

At a constant safety factor q and pressure profile, the plasma kink displacement varies as a function of the applied poloidal mode spectra from the MPs, which we tune through different

Table 2. α exponent factors computed for all ICRH antennas on the basis of the different diagnostics. Results are obtained from OLS and ODR with a 99% confidence interval. The exponents arising from fits to both 2-strap antennas and both 3-strap antennas are highlighted.

Data set	$\alpha_{\mathrm{OLS}} \pm 2.58 \times \sqrt{\mathrm{Var}(\alpha_{\mathrm{OLS}})}$	$\alpha_{\mathrm{ODR}} \pm 2.58 \times \sqrt{\mathrm{Var}(\alpha_{\mathrm{ODR}})}$
ICRH1 (Ref. X4)	8.49 ± 1.40	8.96 ± 0.42
ICRH1 (Lit. Beam)	8.72 ± 2.51	9.04 ± 1.16
ICRH1 (Ref. O)	7.52 ± 2.37	7.91 ± 0.36
ICRH3 (Ref. X4)	5.39 ± 1.63	5.89 ± 0.33
ICRH3 (Lit. Beam)	5.62 ± 1.90	6.01 ± 0.79
ICRH3 (Ref. O)	4.95 ± 1.38	5.30 ± 0.29
ICRH1 and ICRH3 (Ref. X4)	**7.18 ± 0.98**	**7.48 ± 0.37**
ICRH1 and ICRH3 (Lit. Beam)	**7.40 ± 1.90**	**7.57 ± 0.97**
ICRH1 and ICRH3 (Ref. O)	**6.40 ± 1.74**	**6.63 ± 0.32**
ICRH2 (Lit. Beam)	8.03 ± 2.27	8.12 ± 0.50
ICRH2 (Ref. O)	7.49 ± 2.27	7.50 ± 0.26
ICRH4 (Lit. Beam)	7.47 ± 0.53	7.47 ± 0.47
ICRH4 (Ref. O)	6.89 ± 1.32	6.99 ± 0.27
ICRH2 and ICRH4 (Lit. Beam)	**7.79 ± 1.42**	**7.73 ± 0.48**
ICRH2 and ICRH4 (Ref. O)	**7.22 ± 1.70**	**7.14 ± 0.26**

$\Delta\varphi_{\mathrm{UL}}$. In the same fashion as observed in figure 6, the loading resistance variation of each feeder will depend on the plasma displacements. We perform an OLS fit to the loading resistances of each antenna feeder for every one of the applied $\Delta\varphi_{\mathrm{UL}}$ phasings, such that the amplitude of the coupling variation can be obtained. The procedure is displayed in figure 8, where the loading resistances are fitted for the case of $\Delta\varphi_{\mathrm{UL}} = 0°$. The loading resistances for the discharge with no MPs during the same time period are added for comparison. A sliding median filter with a window size of 51 points is performed to the no-MP time traces in order to better visualize the baseline level of the loading. Aside from the harmonic oscillation when the MPs are present, it is also observed that, on average, the loading resistance is higher with MPs than without them, as already observed in previous studies [14, 15]. This observation is consistent with the plasma density increase in the SOL due to the pump-out effect, which is visible in the line-integrated density measurements in figure 3. In the lower plot, we present the loading variation in percentage as a function of the applied $\Delta\varphi_{\mathrm{UL}}$. Here, ΔR_L is the amplitude of the fundamental ν_0 component of each feeder and $\langle R_L \rangle$ is the loading resistance time average of the considered window. Thus, the minimum loading resistance for a given $\Delta\varphi_{\mathrm{UL}}$ is taken to be $\langle R_L \rangle - \Delta R_L$ and the maximum $\langle R_L \rangle + \Delta R_L$. The error bars representing the uncertainty of the OLS fit alone are comparable to the marker size, and thus have not been included. The noise level, marked as a horizontal dashed line on the lower plot, is calculated by performing the same OLS fit to the loading resistances for the discharge with no MPs, and then taking the average over the antenna pairs.

An interesting observation is that the loading resistance baseline increases during the discharge, especially for the 2-strap antennas. This is due to the general electron density increase in the plasma over time, also seen in figure 3. Since the baseline variation is effectively accounted for and removed by the polynomial fit, it is assumed throughout the analysis that the amplitudes of the OLS fit represent an average value of the loading resistance amplitude over the considered time trace. From the performed analysis, a clear dependence of the loading resistance change on the applied $\Delta\varphi_{\mathrm{UL}}$ is observed well above the noise level. This corroborates the picture of the coupling change being directly correlated to the plasma kink displacements. A maximum loading resistance change of ~25% is reached, with a similar $\Delta\varphi_{\mathrm{UL}}$ dependence between the 2-strap antennas and the 3-strap antennas. The 3-strap antennas experience larger coupling changes, as it would be expected from their higher $k_{\parallel} \sim 11\ \mathrm{m}^{-1} > 7.7\ \mathrm{m}^{-1}$ combined with the fact that the displacements decay radially in the SOL. Even larger coupling changes would be expected, well correlated with larger plasma displacements, if the MP field attenuation by the PSL becomes smaller, e.g. with slower MP rotation frequencies, or if larger currents are applied to the MP coils.

3. Experimental scaling of antenna loading resistance with cutoff distance. Comparison to 1D formulas

It is instructive to compare the experimental data obtained in these non-axisymmetric scenarios against one-dimensional analytical and experimentally-derived formulas, often used to describe the scaling behavior of the loading resistance with plasma parameters. In particular, we would like to know if the three-dimensionally perturbed cases behave similarly to radial scans of the (axisymmetric) plasma position in the limit of very small perturbations, and how large does the non-axisymmetry need to become before large deviations occur. For the comparison, we build data sets based on the displacements measured by the different diagnostics. We, therefore, use the density data measured by Ref. X4, Ref. O-mode and the lithium beam for the 2-strap antennas and the Ref. O-mode and lithium beam for the 3-strap antennas. The 1D-cutoff oscillation amplitudes are taken to be $\Delta d_{\mathrm{cutoff}}/2$. Again, we consider $R_L^{(1)} = \langle R_L \rangle - \Delta R_L$ the minimum loading resistance and $R_L^{(2)} = \langle R_L \rangle + \Delta R_L$ the

maximum loading resistance for a given MP phasing. We will also evaluate the data sets for the different ICRF antennas separately and grouped by antenna type. Median values are computed over the feeders of the antennas for each MP phasing and then fitted to an exponential function of the shape $f_{\text{fit}}(d) = e^{-\alpha \Delta d_{\text{cutoff}}}$ from which the α value is obtained. The motivation behind this fitting function stems from the derived expressions in [6, 40]. The radiation impedance of an ICRF antenna depends on the optical properties of the medium in front of it. If an evanescent region exists, we obtain from the cold plasma theory an scaling for the coupling resistance such that:

$$R_c \propto e^{-\beta\eta}, \text{ with } \eta = \int_{\Omega_e} k_\perp dl \tag{6}$$

the optical thickness of the medium, Ω_e the domain that bounds the evanescence region, β a constant that depends on the assumptions made in the derivation and R_c the coupling resistance, equal to the real part of the radiation impedance. In order to evaluate this integral, knowledge of the RF near fields is necessary. Some common approximations rely on stating $|k_\perp| \sim |k_\parallel|$, since in vacuum $|k_\parallel| \gg |k_0|$, with k_0 the free-space wavenumber. Here, we acknowledge the dependence of η on the distance between the strap and the cutoff (size of the coupling region) and retain the functional form $R_L \propto e^{\alpha d_{\text{cutoff}}}$ for convenience. The fitting is performed with two statistical tools: OLS and orthogonal distance regression (ODR). OLS minimizes the squared vertical distance between the fit and the loading resistance measurements in order to determine α. ODR, on the other hand, finds the estimators which minimize the squared errors of the observed points for both the dependent and independent variables $\{k_\parallel \Delta d_{\text{cutoff}}, R_L^{(2)}/R_L^{(1)}\}$. This approach should be more robust than OLS for obtaining the α estimator. The results for both approaches can be visualized in table 2. The covariance matrix is computed both for OLS and ODR, and a 99% confidence interval is constructed assuming the samples to be normally distributed.

Among the mentioned formulas found in the literature, we first turn our attention to the analytically derived one proposed in [6]. This formula is based on the cold plasma dielectric tensor formulation. The plasma is assumed homogeneous in toroidal and poloidal directions and the antenna is assumed perfect, producing a single $k_\parallel$ value. It is further assumed that the only excited plasma mode is the fast wave, and that $n_\perp^2$ increases linearly from the antenna to the R-cutoff within the *linear model* derivation. In order to allow flow of energy from the antenna to the cutoff, the poloidal electric field of the fast wave is decomposed in a sum of two opposite-'propagation' evanescent waves. The coupled power can then be expressed in terms of the plasma admittance, and in the limit of low optical thickness ($0 < \eta < 3$) it reduces to:

$$P_{\text{trans}} \approx P_0 e^{-1.1 k_\parallel d_{\text{cutoff}}} \tag{7}$$

with P_0 the power corresponding to the amplitude of the current at the straps and d_{cutoff} the distance from the antenna to the R-cutoff. Neglecting losses on the antenna conductors and transmission lines, equations (3) and (7) can be used to give an estimate of the loading resistance change due to a radial movement of the cutoff position, Δd_{cutoff}, such that:

$$\Delta R_L = \frac{R_L^{(2)}}{R_L^{(1)}} = e^{-1.1 k_\parallel \Delta d_{\text{cutoff}}}. \tag{8}$$

The results of the comparison between the experimental scaling and this analytical formula can be seen in figure 9. It is observed that the exponent correctly reproduces the experimental data within the given uncertainties for ICRH1, while it overestimates the changes of the other data sets.

We now further compare the data to numerically and experimentally-derived scalings found in the literature. A statistical analysis of the ASDEX Upgrade 2-strap antennas coupling properties, combining L-mode and H-mode discharges, was performed in [15]. The numerically computed coupling resistance (R_c) from the Rsolver code was related to specific features of the experimentally measured density profiles. A scaling law was derived of the shape:

$$R_c \propto e^{-11.5 d_{\text{cutoff}} + 3.9 d_{\min} - 0.064 \nabla_{\text{eff}}} e^{-0.004 \nabla_{\max} + 0.0036 n_{\text{edge}}}, \tag{9}$$

where $d_{\min}$ is the distance between the main R-cutoff and the minimum density gradient, $\min(\nabla n_e)$, used to characterize the effect of the density shoulder that often appears in H-mode density profiles. $\nabla_{\text{eff}} = (n_{\text{edge}} - n_{\text{co}})/(r_{\text{edge}} - r_{\text{co}})$ with n_{edge} defined at the pedestal top following the convention described in [15] and r_{edge} its position, $n_{\text{co}} = 3.5 \times 10^{18}\ \text{m}^{-3}$ the main R-cutoff density for the 2-strap antennas and r_{co} its position. $\nabla_{\max}$ is defined as the maximum density gradient of the profile. A linear relationship was also found between the actual loading resistance as computed by the TOPICA code [42] and the coupling resistance computed by Rsolver, such that $R_L^{\text{TOPICA}} \sim 6.3 R_c^{\text{Rsolver}} - 0.92$. We take the lower limit of this scaling, i.e. $R_L^{\text{approx}} \sim 6.3 R_c^{\text{Rsolver}}$, since it can be shown that $\Delta R_L^{\text{approx}} \leqslant \Delta R_L^{\text{TOPICA}}$ for $R_c^{\text{Rsolver},2}/R_c^{\text{Rsolver},1} \geqslant 1$, yielding:

$$\Delta R_L^{\text{approx}} \propto e^{-11.5 \Delta d_{\text{cutoff}} + 3.9 \Delta d_{\min} - 0.064 \Delta(\nabla_{\text{eff}})} e^{-0.004 \Delta(\nabla_{\max}) + 0.0036 \Delta n_{\text{edge}}}. \tag{10}$$

The evaluation of equation (10) is only possible with a diagnostic that covers the region from the far SOL to the pedestal top. We use lithium beam profiles to give an estimate of the importance of each term in the exponential factor under our experimental conditions. All discharges in table 1 are investigated. We again produce representative profiles analogously to previously performed with the X-mode reflectometers. First, the time traces are ELM-filtered and local maxima and minima density profiles are computed for each MP cycle as the median of the extrema neighboring profiles over ~40 ms. Next, the median is computed again over all the local maxima and minima in order to yield representative profiles for a given $\Delta\varphi_{\text{UL}}$. The result of this procedure is seen in figure 10 for the $\Delta\varphi_{\text{UL}} = 0°$ case. Points for n_{edge}, $\max(\nabla n_e)$, $\min(\nabla n_e)$ are added as per definition in [15]. It is found that in all studied cases $|0.0036 \Delta n_{\text{edge}}| \ll |-11.5 \Delta d_{\text{cutoff}} + 3.9 \Delta d_{\min} - 0.064 \Delta(\nabla_{\text{eff}}) - 0.004 \Delta(\nabla_{\max})|$, and hence can be safely neglected. Among the rest of parameters $|-11.5 \Delta d_{\text{cutoff}}|$ is usually much larger than

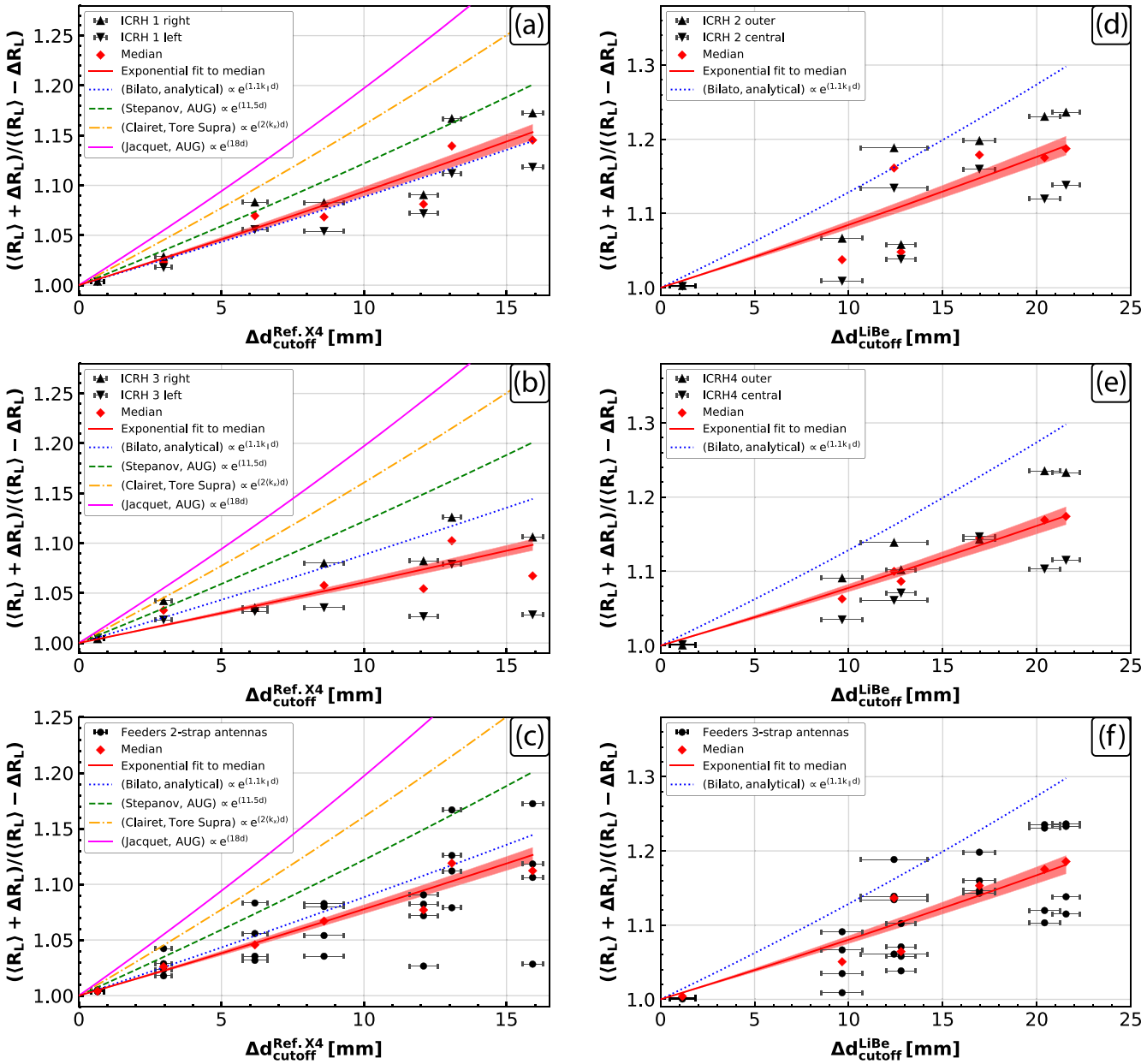

Figure 9. Average change of loading resistance as a function of the average R-cutoff displacement as measured by Ref. X4 for the 2-strap antennas and the lithium beam for the 3-strap antennas. A fit using ODR on f_{fit} is performed. (a)–(c) Using ICRH1 alone, ICRH3 alone and the combined data set. (d)–(f) Using ICRH2 alone, ICRH4 alone and the combined data set. The formula derived in [6] is added as a blue dashed curve. The scaling predicted in [15] is added as a dashed green curve. The scaling predicted in [40] is added as a yellow dashed curve. The scaling measured in [41] is added as a magenta solid curve. The marker size is representative of the vertical OLS 1σ uncertainty.

$\epsilon = |3.9\Delta d_{\text{min}} - 0.064\Delta(\nabla_{\text{eff}}) - 0.004\Delta(\nabla_{\text{max}})|$, except in the cases where Δd_{cutoff} is very small, like in the $\Delta\varphi_{\text{UL}} = 180°$ case, or the density shoulder is not clearly defined and thus cannot be captured by the $\min(\nabla n_e)$ condition. The evaluation of all the MP phases yielded:

$$\left\langle \frac{|-11.5\Delta d_{\text{cutoff}}|}{\epsilon} \right\rangle \sim 24.5 \pm 18.9, \tag{11}$$

where the uncertainty represents 1σ. We hence estimate the main parameter to be Δd_{cutoff} and further reduce $\Delta R_L^{\text{approx}} \sim e^{-11.5\Delta d_{\text{cutoff}}}$. This scaling, which approximates in the lower limit the expected loading resistance change computed by TOPICA for the 2-strap antennas, overestimates the measurements here presented, only agreeing occasionally with some of the feeders as seen in figure 9. Naturally, this scaling can only be applied to the 2-strap antennas, since it was performed prior to the installation of the 3-strap antennas in ASDEX Upgrade and the statistical analysis was never repeated for these.

A purely experimental scaling was also derived for the ASDEX Upgrade 2-strap antennas when studying the influence of different gas puffing locations on the loading resistance [41]. The O-mode reflectometer was utilized to find the distance from the antenna to the R-cutoff, and this was correlated to the loading resistance measured by a set of voltage and current probes in the unmatched transmission lines (not used in this paper). The scaling was derived by uniquely

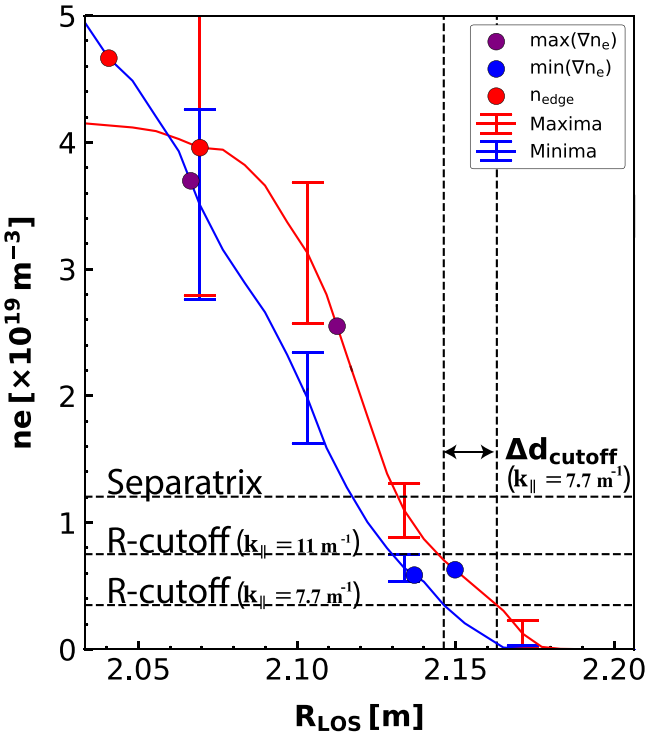

Figure 10. Lithium beam density profiles for discharge #34622, $\Delta\varphi_{UL} = 0°$. Local maxima and minima profiles are computed for each MP cycle taking the median over ~40 ms. The final profiles are computed as the median of all the local extrema profiles.

using H-mode discharges with divertor gas puff. The reported exponent factor was $\alpha \sim 18$, i.e. $\Delta R_L \propto e^{18 d_{\mathrm{cutoff}}}$. This factor greatly overestimates the measured loading resistance for all the antenna feeders. Despite this fact, it will be seen in section 4 that this scaling is in very good agreement with 1D ICRF coupling simulations.

In Tore Supra, the measured loading resistance of a database of ICRF heated discharges could be fit with the exponent $\alpha \sim 17.3$ [40]. This scaling compares favorably to the one found in ASDEX Upgrade ($\alpha \sim 18$), which is further accentuated by the fact that both scalings were obtained with 2-strap antennas, despite the slightly different $k_{\|}$, i.e. $k_{\|}^{\text{Tore Supra}} \sim 9.1\ \mathrm{m}^{-1} > 7.7\ \mathrm{m}^{-1}$. A generalization of the experimental scaling was proposed from purely theoretical grounds stemming from the cold plasma approximation, such that: $R_L \approx e^{-2\langle k_x\rangle d_{\mathrm{cutoff}}}$. Here, $\beta = 2$ and $\eta \sim \langle k_x\rangle d_{\mathrm{cutoff}}$ in equation (6). The value for $\langle k_x\rangle$ was taken to be approximately the maximum $k_{\|}$ of the radiated power spectrum in the plasma, as computed by the ICANT code. The change in loading resistance would be:

$$\Delta R_L = e^{-2\langle k_x\rangle \Delta d_{\mathrm{cutoff}}}. \tag{12}$$

We utilize the RAPLICASOL code as described in the next section in order to better estimate the radiated power $\max(k_{\|})$ for the ASDEX Upgrade 2-strap antenna coupling to an axisymmetric density plasma. We assume the fast wave to carry most of the radiated power, and therefore, we compute the power spectral density (PSD) of the field-aligned RF magnetic field component, which can be seen in figure 13. The vacuum profile is evaluated in the private region in front of the ICRF antenna, close to the FS. The PML profile is evaluated at the end of the simulation domain, where outward radiation boundary conditions exist, and therefore, where we consider the power to be coupled to the core. We have obtained $\max(|k_{\|}^{\mathrm{FS}}|) \sim 7.45\ \mathrm{m}^{-1}$, in good agreement with the value used in the experimental determination of the *R*-cutoff. We therefore approximate $\langle k_x\rangle \sim \max(|k_{\|}^{\mathrm{FS}}|)$ on the basis that $|k_{\|}| \gg |k_0|$, and included this value in the scaling displayed in figure 9. It can be seen that this theory-based scaling also overestimates the measured change in loading resistance.

With the presented comparison, we find that the diverse scalings overestimate the measured loading resistance change in the investigated non-axisymmetric configurations. The best agreement is found with Bilato's scaling for the 2-strap antennas. Nevertheless, this scaling clearly departs from the other experimental and simulation observations reported in the literature. Particularly, it strongly diverges from the experimental 1D scaling in axisymmetric conditions obtained by Jacquet. A marginal improvement can be found if the 2-strap antenna current spectrum $k_{\|}^{\mathrm{current}} \sim 9.25\ \mathrm{m}^{-1}$ is used instead (as suggested in [6]), leading to $R_L \propto e^{10 d_{\mathrm{cutoff}}}$. This departure could be attributed to the assumption that $n_{\perp}^2$ increases linearly from the strap to the cutoff. In reality, it is likely that a sharp decrease in plasma density occurs inside the ICRF limiter. Under these circumstances, the *step model* also proposed in [6] could be a better representation of reality, but has not been here investigated.

It should also be remarked that the experimental scalings here presented were obtained under different (and axisymmetric) plasma conditions, with unknown *S*-matrices, making a comparison with our measured data only qualitative, but still valuable. In addition, we have purposely not included error bars for the scaling laws, since even though they would help to improve the agreement, our objective is simply to compare the experimental data sets against the general trend. We can also attempt to give an explanation to the measured scaling deviation from the ones of the literature in the following manner: in opposition to axisymmetric plasma movements, where the whole plasma column is moved towards/away from the ICRF antenna, the poloidal and toroidal inhomogeneities brought by the MP plasma deformation can make part of the plasma to be closer to the antenna, and another part to be farther away simultaneously with respect to the axisymmetric case. It can be seen in figure 7 that when the plasma is the closest to the antenna center, it is farther away at the antenna top and bottom. An 'integration' of this 3D density structure by the relatively large (compared to the plasma size) ASDEX Upgrade antenna could, therefore, result in a smaller net effect on the coupling characteristics. Thus, one would expect the loading changes to scale slower with the measured 1D cutoff deformation amplitude than those produced by axisymmetric movements of the plasma volume. In other words, if the change in the 3D deformation could be represented by a single 'effective' integrated one-dimensional displacement $\langle \Delta d_{\mathrm{cutoff}}\rangle^{\mathrm{eff}}$, we would likely find $\langle \Delta d_{\mathrm{cutoff}}\rangle^{\mathrm{eff}} < \Delta d_{\mathrm{cutoff}}$. A similar integration was already attempted in [7] for an

axisymmetric plasma with changing triangularity, and when weighted with a filtering factor to account for the exponential evanescent behavior, resulted in a consistent scaling of the measured loading resistance. This approach could also shed some light on why the found radial decay parameters, α, are very similar between the 2-strap and the 3-strap antennas, which is, in principle, an unexpected result due to their different $k_{\|}$. Such study would, however, require precise knowledge of the 3D magnetic topology and needs to be supported by dedicated MHD and/or transport simulations.

It can also be noted that the loading resistance change measured in different feeders scatters more significantly the higher the cutoff oscillation amplitude becomes. Systematic errors in the $V_{\max}$ determination between different feeders can become more apparent the larger the perturbation grows. Furthermore, cross-coupling terms in the unknown *S*-matrices play a role in these differences, which is difficult to asses since no direct measurements of the antennas *S*-matrices are currently possible. However, it is also plausible that the larger scatter between the feeders' experimental data can be partly explained by the poloidal and toroidal effects on coupling becoming of greater importance. In this situation, it is not possible to approximate the coupling change in each feeder accurately with a single 1D scaling anymore (i.e. a single value of Δd_{cutoff}), but rather, a functional description of the *S*-matrix dependence on the 3D density profile becomes mandatory.

In order to better elucidate the impact of arbitrary plasma asymmetries on ICRF coupling, and other important antenna performance quantities, further dedicated 3D experiments and modeling must be performed in the future.

4. ICRF simulations using the COMSOL based RAPLICASOL code

In the previous section, we investigated the scaling of the experimentally measured loading resistance change with respect to the 1D cutoff movements measured by different diagnostics. We found that the derived 1D experimental scaling deviated from previous experimentally-derived and analytical scalings found in the literature. In this section, we focus on the numerical change of the loading resistance when 1D density profiles are fed into an ICRF coupling code. By doing so, we want to test our expectation that considering a 1D density profile for the whole ICRF antenna array, even if representative of the OMP measurements, is not enough to replicate the experimental results, which are inherently of three-dimensional nature. Furthermore, we can test how large the deviation is between the experimental results and the numerical predictions. We will use for the simulations the COMSOL based RAPLICASOL code [43–45]. RAPLICASOL is able to handle the realistic geometry of ICRF antennas, and perform full-wave simulations on a finite element mesh. Maxwell equations are solved in vacuum or plasma conditions, imposed via a dielectric tensor. A 'perfectly matched layer' (PML) provides an absorbing boundary at the radial, toroidal and poloidal ends of the simulation domain, that serves to mimic the outward radiation boundary condition, i.e. no wave reflection. So far, only flat models of the ASDEX Upgrade antennas had been used in RAPLICASOL studies. In order to be as close as possible to the experimental conditions, and to avoid artificial geometric transformations of the density profile from the tokamak toroidal geometry to the usual simulation flat geometry, a new curved model of the ASDEX Upgrade 2-strap antenna has been developed and used, in addition to the usual flat model for comparison. Both models are presented in figure 11.

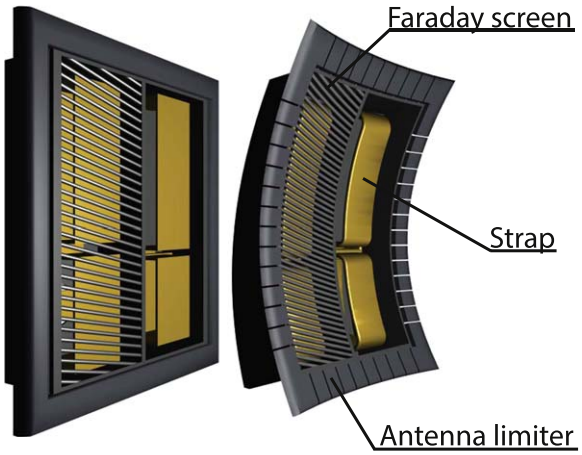

Figure 11. RAPLICASOL flat and curved models of the ASDEX Upgrade 2-strap antenna.

In order to provide representative density profiles for the given experimental conditions, we will use the lithium beam diagnostic, which most extensively covers the ICRF coupling region. We follow the same procedure previously introduced: first, an OLS fit was performed to the ELM-filtered lithium beam time traces for each $\Delta\varphi_{\text{UL}}$, and the time points of local density maxima and minima were found, corresponding to the minimum and maximum antenna-*R*-cutoff gap distance. Second, all density profiles in a given time-window centered at the local extrema are averaged. Third, all the maxima, and, all the minima profiles are averaged together. The time window length is adjusted in order to ensure that the final profiles preserve, as close as possible, the same *R*-cutoffs and separatrix displacements as the ones obtained via OLS in figure 5. A time window of ~40 ms was found to yield the closest agreement between OLS and the profile reconstruction procedure. Since the angle between the lithium beam LOS and the normal vector to the axisymmetric separatrix is of the order of $\alpha^{\text{libe}} \sim 20°$, $\cos(\alpha^{\text{libe}}) \sim 0.94$, this is regarded as a second-order contribution and has not been corrected for in the reconstruction. The resulting density profiles are displayed in figure 12.

We now compute with the curved antenna model the PSD of the field-aligned RF magnetic field component, which can be seen in figure 13. The obtained $\max(k_{\|}) \sim 7.45\ \text{m}^{-1}$ in the vacuum region is in good agreement with previous HFSS models of the ASDEX Upgrade 2-strap antennas [20], giving confidence in its robustness. Furthermore, we have constructed

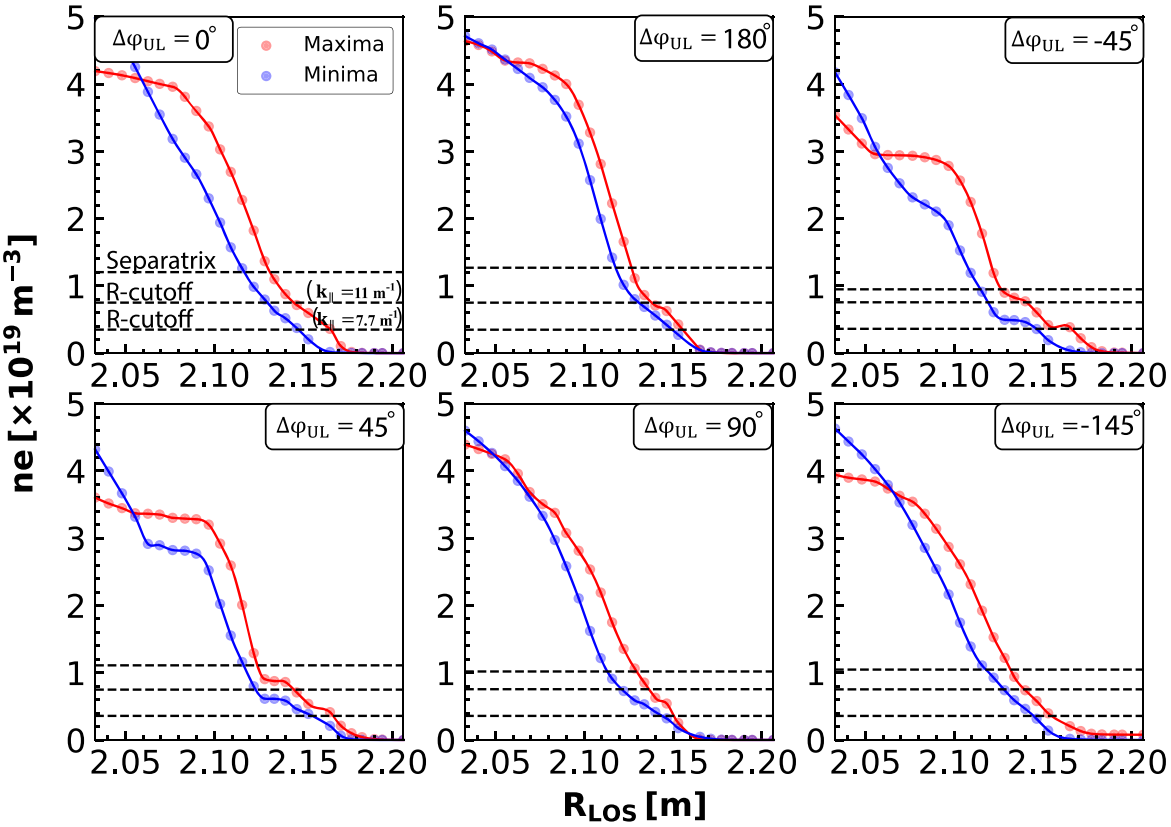

Figure 12. $n_e = f(\Delta\varphi_{\mathrm{UL}})$ profiles computed from the lithium beam diagnostic. (Red) Maximum, i.e. closest approach of the plasma to the ICRF antenna, (blue) minimum, i.e. largest separation between the plasma and the ICRF antenna. Separatrix and *R*-cutoff densities are computed for each case and marked as dashed lines.

this RAPLICASOL model following a CAD design of the actual ASDEX Upgrade 2-strap antenna, and the geometrical features were further compared with the antenna used in the TOPICA code.

The coupling simulations were performed by considering a 1D induction field varying as $|B| \propto |B_0|R_0/R$, with $|B_0| = 2.5$ T the on-axis induction field, and $R_0 = 1.65$ m the torus major radius. A constant induction field angle of 11° is imposed over the simulation domain, in the tilt direction of the FS bars. In the future, this simplification can be removed by adding a realistic field from a non-axisymmetric MHD equilibrium calculation. Vacuum conditions are imposed in the domain bounded by the outer wall and $n_e = 1 \times 10^{17}\ \mathrm{m}^{-3}$ in order to avoid the lower hybrid resonance, which cannot be handled with the COMSOL finite element formulation. A maximum density of $n_e^{\max} = 2.5 \times 10^{19}\ \mathrm{m}^{-3}$ is set in the plasma domain in order to ensure no density gradients exist in the plasma-PML interface. The curved model is run with the direct solver, whereas the flat model is converged with the iterative solver, setting 1% relative tolerance. The mesh was set with hexahedral elements of a characteristic radial length of ∼1 cm for the curved model, whereas the flat model uses tetrahedral elements with a radial length of ∼2 cm. Both resolutions should be enough to resolve the perpendicular wavelength of the fast wave in the coupling region, which for our conditions is of the order of $\min(|\lambda_\perp|) \sim 15$ cm. Two sets of simulations are performed: using the profiles in figure 12 for comparison between the maximum and minimum approach to the ICRF antenna per MP phasing, and a radial scan using only the density profile for $\Delta\varphi_{\mathrm{UL}} = 0°$ 'maxima'. The radial scan was performed by outward shifting the density profile in steps of 4 mm and thickening the vacuum layer in each iteration by the same width. With these two sets, we are able to distinguish between loading resistance changes due to a pure radial shift of the density profile from coupling changes that include variation in the density gradients. The computed S-matrices are transformed into loading resistances by assuming a perfect coaxial line with $Z_0 = 25\ \Omega$ characteristic impedance, such that [46]:

$$\begin{pmatrix} V_r^1 \\ V_r^2 \end{pmatrix} = \begin{pmatrix} S_{11} & S_{12} \\ S_{21} & S_{22} \end{pmatrix} \begin{pmatrix} V_f^1 \\ V_f^2 \end{pmatrix} \tag{13}$$

with V_r^i the reflected voltage and V_f^i the forward voltage on port i, and S_{ij} the S-matrix elements. We impose $V_f^1 = V_f^2$ in our simulations, such that:

$$|\Gamma_i| = |S_{ii} + S_{ij}|, \quad \mathrm{VSWR}_i = \frac{1 + |\Gamma_i|}{1 - |\Gamma_i|}$$
$$R_L^i = \frac{Z_0}{\mathrm{VSWR}_i}. \tag{14}$$

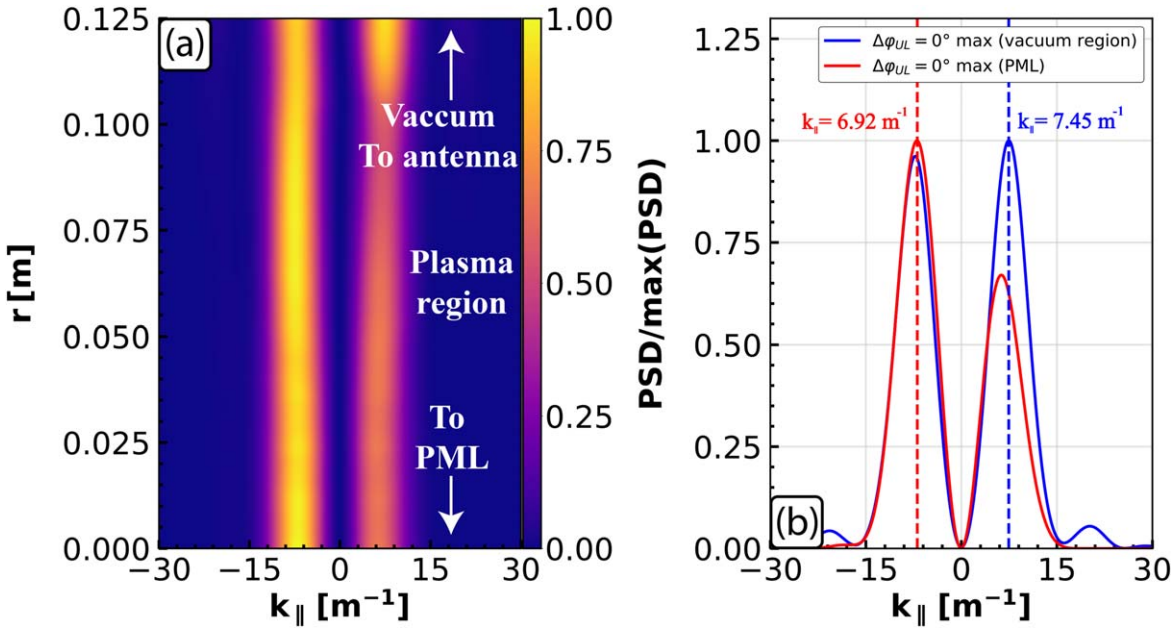

Figure 13. (a) PSD of the RF magnetic field component for a field-aligned 2D plane intersecting the coupling region. (b) PSD as in (a) for $r = 0.125$ m (inside the vacuum region) and $r = 0$ m at the plasma-PML interface.

We present the simulation results, alongside with the scaling laws introduced in the previous section in figure 14. Since the utilized antenna model intends to represent either of the real ASDEX Upgrade 2-strap antennas, the simulated loading resistance values for both feeders are averaged, and compared against the experimental median value corresponding to the combined data set of ICRH1 and ICRH3. The *R*-cutoff displacement as measured by Ref. X4 for a given experimental point is used to evaluate the scaling laws. A linear regression is performed in order to better visualize differences between the multiple approaches, of which the linear estimators are listed in table 3. While the correct scaling behavior is reproduced with RAPLICASOL, i.e. the simulations of loading resistance change converge to 1, as $\Delta d_{\text{cutoff}} \rightarrow 0$, the predicted change exceeds that of experiments by a factor of $\sim$3 for both the curved and flat models. The radial scans display a similar scaling to that obtained when using the full density profiles. We also find that the experimental scaling proposed by Jacquet for the ASDEX Upgrade 2-strap antennas in axisymmetric plasma radial scans is in excellent agreement with the 1D simulations. This observation further validates the RAPLICASOL results, and supports the conclusion obtained in the previous section.

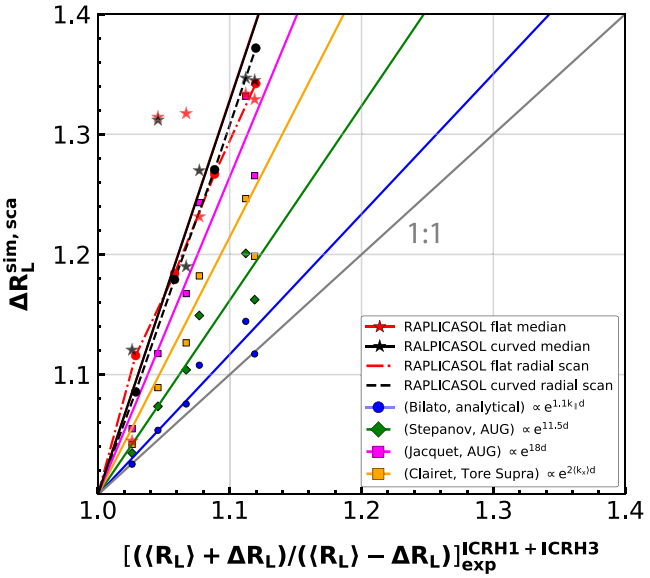

Figure 14. Change in loading resistance from RAPLICASOL (sim) and scaling laws (sca), $\Delta R_L^{\text{sim,sca}}$, versus experimental median values of the ICRH1 and ICRH3 combined data set.

5. 1D empirical extrapolation to the ITER ICRF system

It has been shown in table 2 that the experimentally-derived ODR exponents for the combined data sets of 2-strap and 3-strap antennas are very similar. This is despite the fact that the two types of ICRF antennas have different geometry, $k_{\parallel}$ wavenumber spectra and thus *R*-cutoff positions. We can take advantage of this fact to forecast the average coupling change of an ASDEX-like ICRF antenna in an ITER-like plasma. This exercise is meant to provide an overview of the similarities and differences between both machines, and will highlight the main knowledge gaps that need to be bridged in the future.

We will use the same scaling function with the experimentally-derived radial decay parameter α. If each of the derived α from the combined 2-strap and 3-strap data sets are taken to be independent realizations, and assume α normally

Table 3. Linear estimators for the different scalings and RAPLICASOL simulations. Results using OLS with a 99% confidence interval.

Approach	Linear estimator
Bilato's formula, $k_{\|} = 7.7\ \mathrm{m}^{-1}$	1.168 ± 0.183
Stepanov's scaling (lower limit)	1.617 ± 0.255
Clairet's scaling, $\langle k_x \rangle \sim \lvert k_{\|}^{\mathrm{FS}} \rvert = 7.45\ \mathrm{m}^{-1}$	2.144 ± 0.343
Jacquet's scaling	2.644 ± 0.428
RAPLICASOL flat model simulations	3.286 ± 1.207
RAPLICASOL flat model radial scan	2.978 ± 0.282
RAPLICASOL curved model simulations	3.276 ± 1.021
RAPLICASOL curved model radial scan	3.080 ± 0.035

distributed, we can construct a 99% confidence interval based on the standard deviation of these realizations, which yields:

$$\begin{cases} \langle \Delta R_L^{\mathrm{MP}} \rangle \sim e^{\langle \alpha^{\mathrm{MP}} \rangle \Delta d_{\mathrm{cutoff}}} \\ \langle \alpha^{\mathrm{MP}} \rangle = 7.31 \pm 1.01 \end{cases} \tag{15}$$

with $\langle \alpha^{\mathrm{MP}} \rangle$ the average of the ODR exponents for the combined data sets of 2-strap and 3-strap antennas. There are no, as of currently, predictions for the *R*-cutoff displacement in ITER, but they do exist for the separatrix. We will take these as a reference, but bearing in mind that the actual *R*-cutoff displacements may be smaller/bigger depending on SOL conditions. Different models have been used to predict such midplane displacements. In [47] displacements ranging from ± 2 to ± 3.5 cm are discussed in base of the modeling approach taken (vacuum field-line tracing, ideal MHD modeling and resistive linear and nonlinear modeling) and the kinetic profiles used, such as the electron pedestal temperature. This translates to our particular case in displacements ranging from $\Delta d_{\mathrm{separatrix}} = 4 - 7$ cm from the minimum to the maximum separatrix position at full coil-current (90 kAt). We will take these as our upper-estimation, since it is clear that reducing the coil currents, should ELM mitigation/suppression be achieved in such conditions, would produce the displacements to consequently decrease. The resulting coupling variation in % is shown in figure 15. The dependence on the excited $k_{\|}$ spectrum by the antenna enters this equation implicitly via $\Delta d_{\mathrm{cutoff}}$. In ITER, we expect spectra ranging from $\max(k_{\|}) \sim 2 - 6\ \mathrm{m}^{-1}$, the minimum corresponding to $\{0, 0, \pi, \pi\}$ phasing, the maximum to $\{0, \pi, 0, \pi\}$ for $\{0, \pi\}$ poloidal phasing [48]. The latter is close to the 2-strap antenna case in ASDEX Upgrade, and it is expected to have the largest coupling variation assuming a monotonically decreasing displacement profile from the separatrix to the wall. It is likely, however, that the most used configuration will lie in between $k_{\|} \sim 3 - 4\ \mathrm{m}^{-1}$, as the $\{0, \pi, \pi, 0\}$ phasing might help reduce ICRF-specific impurity production when the toroidal straps are properly balanced power-wise [49].

When extrapolating this scaling to the ITER ICRF antenna, there exist two main factors that can affect the prediction. First, it is expected from theory that the lower $k_{\|}$ becomes, the smaller α should be. In the discussed range of $k_{\|} \sim 2 - 6\ \mathrm{m}^{-1} < 7.7 - 11\ \mathrm{m}^{-1}$, the value for $\langle \alpha^{\mathrm{MP}} \rangle$ here used will likely represent an overestimation. This lower $k_{\|}$ also has the benefit of producing smaller $\Delta d_{\mathrm{cutoff}}$. On the other hand, in ASDEX Upgrade the vertical size relation between the plasma confined region and ICRF antenna is $\lambda_r^{\mathrm{AUG}} \sim 1.6{:}\ 1$, assuming an elongated radius ~ 0.8 m. In ITER this size relation becomes $\lambda_r^{\mathrm{ITER}} \sim 7{:}\ 2 \sim 2.2 \times \lambda_r^{\mathrm{AUG}}$ [50]. Non-axisymmetric features that might be 'integrated' by the ASDEX Upgrade antennas will appear as a more homogeneous perturbation in front of the ITER antenna, raising the expected value of $\langle \alpha^{\mathrm{MP}} \rangle$ closer to the axisymmetric one. Seen from other perspective, we should expect that in ITER $\langle \Delta d_{\mathrm{cutoff}} \rangle^{\mathrm{eff}} \to \Delta d_{\mathrm{cutoff}}$. Thus, the expectation of smaller loading changes than those predicted by equation (15) due to the smaller $k_{\|}$ in ITER can be overturned by a larger effective displacement than that in ASDEX Upgrade.

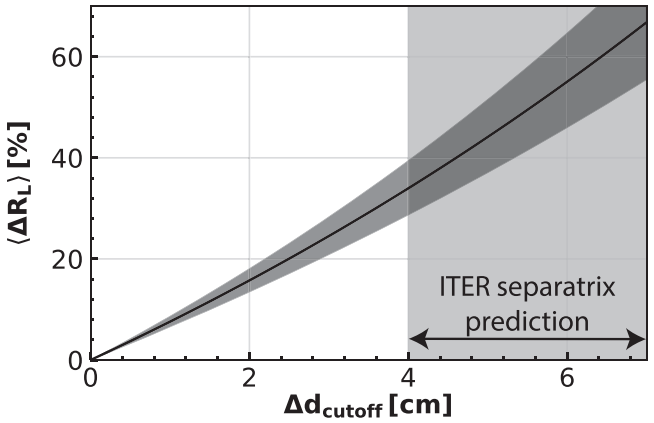

Figure 15. Average loading resistance change (%) as a function of the cutoff displacement. A prediction for the separatrix displacement from the minimum to the maximum plasma clearance is marked with a gray highlight.

Other uncertainty factors include the fact that this scaling has been constructed uniquely with $n = 2$ MP symmetry, and a plasma edge safety factor $q_{95} \sim 5.3$. Predictions for the ITER boundary displacement include $n = 3$ and $n = 4$ symmetric configurations, which will display a different perturbation poloidal mode number at the edge as a function of the ITER *q*-profile. Additionally, a finite k_θ due to poloidal strap phasing, antenna up-down asymmetry and cross-coupling will also play a role.

6. Conclusions

In this study, we have systematically explored for the first time the effect of rotating MPs on the ICRF fast wave coupling performance. In this manner, we have addressed two physical goals: the controlled study of the effect of 3D perturbations on the ICRF system (mimicking external MHD modes, and giving insight into stellarator geometry), and the actual effect of MPs on the ICRF system. The plasma confined region response to the MPs creates a field-aligned kink displacement which depends on the plasma conditions and the applied poloidal spectra, $\Delta\varphi_{\mathrm{UL}}$, in the MP current waveforms. The plasma displacements decay

monotonically in the SOL, registered by the lithium beam and reflectometry diagnostics. However, the SOL can be noticeably affected by local sources and sinks, meaning that the SOL displacement dependence on $\Delta\varphi_{\mathrm{UL}}$ might not correspond to that of the separatrix.

The loading resistance measured in each ICRF antenna feeder reacts accordingly to the SOL density modification, well diagnosed by embedded X-mode reflectometry in three different poloidal positions. Two overlapping effects participate in the loading resistance changes: the plasma pump-out effect, seen as an average increase of the loading resistance with respect to a reference discharge with no MPs, and the rotating kink displacement, seen as a coherent oscillation of the loading resistance locked to the MP rotation. The maximum change in loading resistance is experienced approximately when the density profile is shifted closer/farther to the antenna center. For the studied cases in ASDEX Upgrade, the net effect is an increase of the overall loading resistance at the expense of time variable coupling conditions. For the first time, it is reported that the loading resistance changes do depend on the poloidal phasing of the MPs. A 1D scaling is derived that relates the change in the distance between the ICRF antenna and fast wave *R*-cutoff, as measured by several diagnostics, to the average change in loading resistance. This scaling is seen to predict smaller average loading resistance changes with $\Delta d_{\mathrm{cutoff}}$ than that of scalings previously reported in the literature. It is plausible that the underlying reason is the 'integration' by the ICRF antenna over the whole 3D perturbed density profile, which would result in a milder loading resistance change than that produced by axisymmetric plasma movements.

ICRF simulations are performed with the 3D full-wave solver RAPLICASOL code. The input density profiles have been reconstructed from the lithium beam diagnostic. The magnetic induction field is treated in 1D approximation, decaying with $1/R$. The predicted loading resistance changes exceed that of experiments by a factor of $\sim$3 when using either the curved or flat ASDEX Upgrade 2-strap antenna models. This prediction is in very good agreement with previous coupling studies evaluated in axisymmetric plasma conditions and highlights the need to treat the problem in a full 3D fashion, as the reduction to 1D prevents predictive capabilities.

The experimentally-derived scaling exponent is utilized for a prediction of the change in loading resistance for the ITER ICRF antenna in MP active plasmas. This scaling predicts changes up to $\langle \Delta R_L \rangle \sim 65\%$ when the *R*-cutoff displacement can be identified with the maximum predicted separatrix displacement by different MHD simulations. However, this scaling allows only to give an estimation on the average array behavior, and not on the individual straps, for which the *S*-matrices need to be known. Furthermore, it is expected that the lower $k_{\|}$ value used in ITER and the relative size increase between the ITER plasma and ICRF antenna of $\lambda_r^{\mathrm{ITER}} \sim 2.2 \times \lambda_r^{\mathrm{AUG}}$ will affect this prediction. In order to diagnose the full effect of MPs on the ITER ICRF system, where a complex interplay exists among the 8 strap triplets, and the ratio between ICRF antenna size to the plasma perturbation characteristic wavelength in the midplane is different from ASDEX Upgrade, the problem needs to be addressed by considering a 3D magnetic field, density and antenna model altogether. Lastly, we would like to point out that coupling oscillations such as the ones presented in this study can have implications for antennas working close to their operational limits. If the plasma cutoff displacement becomes large enough to revert the benefit of the induced pump-out, the loading resistance can decrease below the level with no MPs for some rotation phases. This would lead to higher voltages in the antenna structure. Nevertheless, such a situation has not been observed in the studied scenarios.

Overall, the data here presented should help clarify the possible impact of plasma asymmetries on the total delivered RF power to the core plasma, help improve the matching and controller strategy, as well as shed some light on the implications on RF image current compensation on ICRF limiters.

Acknowledgments

This work has been carried out within the framework of the EUROfusion Consortium and has received funding from the Euratom research and training program 2014–2018 and 2019–2020 under grant agreement No 633053. The views and opinions expressed herein do not necessarily reflect those of the European Commission.

ORCID iDs

G Suárez López https://orcid.org/0000-0001-9009-0027
L Guimarãis https://orcid.org/0000-0001-5764-6329
R McDermott https://orcid.org/0000-0002-8958-8714

References

[1] Eugene H 2002 *Optics* (Reading, MA: Addison-Wesley)
[2] Ram A and Bers A 1984 Coupling theory for ICRF heating of large tokamaks *Nucl. Fusion* **24** 679–95
[3] Stix T H 1992 *Waves in Plasmas* (New York: AIP)
[4] Brambilla M 1998 *Kinetic Theory of Plasma Waves* (Oxford, UK: Clarendon Press)
[5] Bobkov V 2003 Studies of high voltage breakdown phenomena on ICRF (Ion Cyclotron Range of Frequencies) antennas *PhD Thesis* Ghent University
[6] Bilato R *et al* 2005 Influence of an evanescence layer in front of the antenna on the coupling efficiency of ion cyclotron waves *Nucl. Fusion* **45** L5
[7] Bobkov V V *et al* 2006 ICRF antenna coupling dependence on edge plasma conditions in ASDEX Upgrade *Nucl. Fusion* **46** S469–75
[8] Zhang W *et al* 2016 3D simulations of gas puff effects on edge density and ICRF coupling in ASDEX Upgrade *Nucl. Fusion* **56** 036007
[9] Zhang W *et al* 2017 Effects of outer top gas injection on ICRF coupling in ASDEX Upgrade: towards modelling of ITER gas injection *Plasma Phys. Control. Fusion* **59** 075004

[10] Ongena J *et al* 2014 Study and design of the ion cyclotron resonance heating system for the stellarator Wendelstein 7-X *Phys. Plasmas* **21** 061514

[11] Huijsmans G T A *et al* 2015 Modelling of edge localised modes and edge localised mode control *Phys. Plasmas* **22** 021805

[12] Mukherjee A *et al* 2015 Status of R&D activity for ITER ICRF power source system *Fusion Eng. Des.* **96–97** 542–6

[13] Ikeda K 2007 Progress in the ITER physics basis *Nucl. Fusion* **47** S1–403

[14] Bobkov V *et al* 2014 Influence of gas injection location and magnetic perturbations on ICRF antenna performance in ASDEX Upgrade *AIP Conf. Proc.* **1580** 271–4

[15] Stepanov I 2015 Ion cyclotron range of frequencies (ICRF) power coupling and plasma density profile *PhD Thesis* Ghent University

[16] Suárez López G *et al* 2017 Investigation of the coupling properties of the ion cyclotron fast wave under applied magnetic perturbations and MHD phenomena in ASDEX Upgrade *EPJ Web Conf.* **157** 03051

[17] Hirshman S P and Whitson J C 1983 Steepest-descent moment method for three-dimensional magnetohydrodynamic equilibria *Phys. Fluids* **26** 3553

[18] Hirshman S P, van Rij W I and Merkel P 1986 Three-dimensional free boundary calculations using a spectral Green's function method *Comput. Phys. Commun.* **43** 143–55

[19] Bobkov V *et al* 2017 Making ICRF power compatible with a high-Z wall in ASDEX Upgrade *Plasma Phys. Control. Fusion* **59** 014022

[20] Bobkov V *et al* 2016 First results with 3-strap ICRF antennas in ASDEX Upgrade *Nucl. Fusion* **56** 084001

[21] Willensdorfer M *et al* 2016 Plasma response measurements of external magnetic perturbations using electron cyclotron emission and comparisons to 3D ideal MHD equilibrium *Plasma Phys. Control. Fusion* **58** 114004

[22] Willensdorfer M *et al* 2017 Three dimensional boundary displacement due to stable ideal kink modes excited by external $n = 2$ magnetic perturbations *Nucl. Fusion* **57** 116047

[23] Shafer M W *et al* 2014 Plasma response measurements of nonaxisymmetric magnetic perturbations on DIII-D via soft x-ray imaging *Phys. Plasmas* **21** 122518

[24] Ham C J *et al* 2014 Modelling of three dimensional equilibrium and stability of MAST plasmas with magnetic perturbations using VMEC and COBRA *Phys. Plasmas* **21** 102501

[25] Sauter O, Angioni C and Lin-Liu Y R 1999 Neoclassical conductivity and bootstrap current formulas for general axisymmetric equilibria and arbitrary collisionality regime *Phys. Plasmas* **6** 2834–9

[26] Hager R and Chang C S 2016 Gyrokinetic neoclassical study of the bootstrap current in the tokamak edge pedestal with fully non-linear Coulomb collisions *Phys. Plasmas* **23** 042503

[27] Fischer R *et al* 2010 Integrated data analysis of profile diagnostics at ASDEX Upgrade *Fusion Sci. Technol.* **58** 675–84

[28] McDermott R M *et al* 2018 Evaluation of impurity densities from charge exchange recombination spectroscopy measurements at ASDEX Upgrade *Plasma Phys. Control. Fusion* **60** 095007

[29] Suttrop W *et al* 2018 Experimental conditions to suppress edge localised modes by magnetic perturbations in the ASDEX Upgrade tokamak *Nucl. Fusion* **58** 096031

[30] Willensdorfer M *et al* 2014 Characterization of the Li-BES at ASDEX Upgrade *Plasma Phys. Control. Fusion* **56** 025008

[31] Viezzer E *et al* 2012 High-resolution charge exchange measurements at ASDEX Upgrade *Rev. Sci. Instrum.* **83** 103501

[32] Aguiam D E *et al* 2016 Implementation of the new multichannel X-mode edge density profile reflectometer for the ICRF antenna on ASDEX Upgrade *Rev. Sci. Instrum.* **87** 11E722

[33] Silva A *et al* 1996 Ultrafast broadband frequency modulation of a continuous wave reflectometry system to measure density profiles on ASDEX upgrade *Rev. Sci. Instrum.* **67** 4138–45

[34] Carralero D *et al* 2017 A study on the density shoulder formation in the SOL of H-mode plasmas *Nucl. Mater. Energy* **12** 1189–93

[35] Mazzucato E 1998 Microwave reflectometry for magnetically confined plasmas *Rev. Sci. Instrum.* **69** 2201–17

[36] McCarthy P J, Martin P and Schneider W 1999 *The CLISTE interpretive equilibrium code Technical Report* Max-Planck-Institut für Plasmaphysik, Garching (http://hdl.handle.net/11858/00-001M-0000-0027-6023-D)

[37] Aguiam D E *et al* 2018 Implementation of the new multichannel Xmode edge density profile reflectometer for the ICRF antenna on ASDEX Upgrade *PhD Thesis* Universidade de Lisboa, Ghent University

[38] Bobkov V *et al* 2013 ICRF operation with improved antennas in ASDEX Upgrade with W wall *Nucl. Fusion* **53** 93018

[39] Rott M *et al* 2009 Electro-magnetic modeling of the planned active invessel coils at ASDEX upgrade *Fusion Eng. Des.* **84** 1653–7

[40] Clairet F *et al* 2004 ICRF coupling and edge density profile on Tore Supra *Plasma Phys. Control. Fusion* **46** 1567–80

[41] Jacquet P *et al* 2016 Maximization of ICRF power by SOL density tailoring with local gas injection *Nucl. Fusion* **56** 46001

[42] Milanesio D *et al* 2009 A multi-cavity approach for enhanced efficiency in TOPICA RF antenna code *Nucl. Fusion* **49** 115019

[43] Jacquot J *et al* 2017 Sequential modelling of ICRF wave near RF fields and asymptotic RF sheaths description for AUG ICRF antennas *EPJ Web Conf.* **157** 03020

[44] Colas L *et al* 2017 SOL RF physics modelling in Europe, in support of ICRF experiments *EPJ Web Conf.* **157** 01001

[45] Tierens W *et al* 2019 Validation of the ICRF antenna coupling code RAPLICASOL against TOPICA and experiments *Nucl. Fusion* **59** 046001

[46] Orfanidis S J 2016 *Electromagnetic Waves and Antennas* (online: copyright 1999–2016 S J Orfanidis) (www.ece.rutgers.edu/~orfanidi/ewa)

[47] Chapman I T *et al* 2014 Three-dimensional distortions of the tokamak plasma boundary: boundary displacements in the presence of resonant magnetic perturbations *Nucl. Fusion* **54** 083006

[48] Milanesio D and Maggiora R 2010 ITER ICRF antenna analysis and optimization using the TOPICA code *Nucl. Fusion* **50** 025007

[49] Bobkov V *et al* 2019 Impact of ICRF on the scrape-off layer and on plasma wall interactions: from present experiments to fusion reactor *Nucl. Mater. Energy* **18** 131–40

[50] Budny R *et al* 2012 Benchmarking ICRF full-wave solvers for ITER *Nucl. Fusion* **52** 023023